

Research Article

Simulation-augmented learning for ballistic performance prediction of ultra-high-strength steel

Qichao Wei¹, Pingluo Zhao^{1,2,3,*}, Qiang Hao¹, Wuguo Chen⁴, Hongmei Zhang^{1,2,3}, Yangwei Wang^{1,2,3}, Xingwang Cheng^{1,2,3,*}

¹National Key Laboratory of Science and Technology on Materials Under Shock and Impact, School of Materials Science and Engineering, Beijing Institute of Technology, Beijing 100081, China.

²Materials Intelligent Innovation Laboratory, Beijing Institute of Technology, Zhuhai 519088, Guangdong, China.

³Tangshan Research Institute, Beijing Institute of Technology, Tangshan 063000, Hebei, China.

⁴Institute of Equipment Lightweighting, Beijing Institute of Technology Chongqing Innovation Center, Chongqing 401120, China.

***Correspondence to:** Dr. Pingluo Zhao, Prof. Xingwang Cheng, National Key Laboratory of Science and Technology on Materials Under Shock and Impact, School of Materials Science and Engineering, Beijing Institute of Technology, Beijing 100081, China; Materials Intelligent Innovation Laboratory, Beijing Institute of Technology, Zhuhai 519088, Guangdong, China; Tangshan Research Institute, Beijing Institute of Technology, Tangshan 063000, Hebei, China. E-mail: zhaopingluo@bit.edu.cn; chengxw@bit.edu.cn

How to cite this article: Wei Q, Zhao P, Hao Q, Chen W, Zhang H, Wang Y, Cheng X. Simulation-augmented learning for ballistic performance prediction of ultra-high-strength steel. *J Mater Inf* 2026;6:[Accept]. <http://dx.doi.org/10.20517/jmi.2025.95>

Received: 22 December 2025 | **Revised:** 6 May 2026 | **Accepted:** 7 May 2026

Abstract

Direct measurement of ballistic service performance in extreme-service materials is costly and data-limited because penetration testing requires specialized facilities and yields only a small number of valid observations. This limitation makes it difficult to establish reliable links between routine mechanical properties and terminal ballistic responses. To address this gap, we propose a simulation-augmented two-stage learning framework that maps standard mechanical-test results to service-level ballistic responses under small-sample conditions. The framework first identifies the Johnson-Cook (JC) constitutive and failure parameters, together with a pressure-cutoff criterion, from limited experiments using chaos-based global optimization. The identified parameters are then used to perform high-throughput penetration simulations, thereby augmenting the scarce experimental service data. The augmented dataset is processed using a two-stage learner, in which random forests classify discrete outcomes and a multilayer perceptron regression predicts continuous metrics. In a case study of G33 ultra-high-strength steel, the optimized feature-selected model achieved cross-validated prediction accuracies of 98.3%, 74.8%, 92.9%, and 89.8% for penetration occurrence, post-penetration projectile integrity, residual velocity, and critical projectile fragmentation velocity, respectively. The proposed framework provides a transferable strategy for ballistic performance prediction in other impact-dominated material systems with limited service data.

Keywords: Extreme service materials, materials informatics, simulation-efficient learning, two-stage modeling, ultra-high-strength steel, chaos optimization algorithm

INTRODUCTION

Ultra-high-strength steels, which optimally balance high strength with adequate toughness, are essential for critical components subjected to extreme stresses. This exceptional profile has driven its widespread use in heavy industries. In the aerospace industry, these steels are critical constituents of high-load elements such as landing gears, main wing beams, and horizontal stabilizer spars^[1-3]. Similarly, the automotive sector utilizes these steels in car frames, crash beams, and A- and B-pillars to deliver cost-effective safety and durability^[4-6]. Driven by increasingly stringent engineering demands, the steel industry has continuously developed innovative ultra-high-strength steels^[7,8]. An example is G33 ultra-high-strength steel, which integrates bainitic and

martensitic design principles to achieve an excellent balance of strength and toughness at a reduced cost. However, because its properties are highly sensitive to heat, it is critical to quantify the extent to which specific processing routes dictate the mechanical and service behaviors. Consequently, a pressing need exists for rapid and cost-effective methods to evaluate the terminal performance of advanced steels^[9,10].

In the digital era, material genome engineering has emerged as a primary driver of data-driven materials research. The launch of the Materials Genome Initiative in 2011 marked a major step toward data-centric strategies in materials science^[11] and accelerated the adoption of big data and artificial intelligence in the field^[12,13]. This paradigm relies on the systematic collection, analysis, and interpretation of large datasets of materials to support the optimization and evaluation of new materials. For example, Yang *et al.* reviewed recent progress in data-driven materials research from the perspectives of functional material design and guided synthesis, and highlighted common indicators and methods for property design and synthesis-route prediction^[14]. Merayo *et al.* developed a large data-driven artificial neural network system to predict the physical and mechanical properties relevant to the selection of metallic materials^[15]. Guo *et al.* proposed a machine-learning-based nonlinear programming approach for predicting multiple properties of steels from industrial big data^[16]. Taken together, these studies demonstrate the growing potential of advanced data analytics in accelerating material design and performance prediction.

However, experimental constraints, technological limitations in characterization, and data complexity pose significant challenges to data acquisition. For instance, high-cost, complex experimental designs are necessary to obtain data on service performance attributes such as penetration ability and fatigue life^[17]. These complications are exemplified by the efforts of researchers such as He *et al.*, who developed complex geometries for high-speed penetrators, including detailed specifications of the total length, nose and rod sections, and various diameters. Data collection involved the use of high-speed cameras to measure the free-flight speed and impact behavior of these penetrators, all of which necessitated a substantial investment^[18]. In studies conducted by Kılıç *et al.*, ballistic tests on high-hardness armor plates using Secure 500 steel and 7.62×54 mm B32 API armor-piercing bullets were performed according to NATO

Stanag 4569 level 3 standards. Their meticulous recordings of the bullet speed and target interactions using synchronized high-speed cameras and precise timers entailed intricate data collection processes and expensive equipment^[19]. An additional example of the complexity and high costs of experimental designs is the work of Børvik *et al.*, who conducted penetration tests on granular materials with various small-caliber bullets, totaling 126 experiments^[20].

Attempts to lower the costs of complex and expensive experimental settings have resulted in the emergence of finite-element simulations as an efficient alternative that enables the rapid acquisition of material performance data through the precise simulation of actual test conditions. Nonetheless, the interplay of multiple simulation parameters and the accumulation of errors from testing and fitting pose significant obstacles to accurately determining simulation parameters. For example, Manes *et al.* combined experimental and simulation approaches using ABAQUS and LS-DYNA to study the penetration and perforation behaviors of aluminum plates of varying thicknesses. They focused on a multitude of simulation parameters such as different friction coefficients, impact speeds, and the characteristics of the projectile and target materials^[21]. Zhu *et al.*, who used the Johnson-Cook (JC) strength model to simulate the penetration performance of depleted uranium alloys, considered a variety of simulation parameters, including the equivalent stress, equivalent strain, strain rate, homologous temperature, material melting point, room temperature, yield stress, strain hardening coefficient, and temperature softening coefficient^[22]. These efforts suggest that an investigation of the structure-performance relationship between the mechanical properties and service performance of G33 ultra-high-strength steel would require an efficient method for deriving the simulation parameters. A comprehensive dataset can be built by conducting batch parallel simulation calculations to support the data-driven predictions of the material performance.

This study aims to rapidly assess the service performance of metal by learning the nonlinear mapping from conventional mechanical properties (for example, the yield strength) to service behavior (for example, the penetration performance) using G33 ultra-high-strength steel as a case study. We prepared 134 microstructures using various heat-treatment methods and measured their mechanical properties at different temperatures and strain rates, which were then used to construct a comprehensive

dataset comprising these properties. Subsequently, using limited penetration test data and techniques, such as chaotic optimization, we determined the key simulation parameters for all 134 variants, which made it possible to construct an extensive service performance dataset. Based on these data, we developed a two-stage prediction framework that uses random forests for discrete outcomes and multilayer perceptrons for continuous metrics. Unlike conventional single-stage models, which have difficulties accommodating sharp discontinuities at the ballistic limit, the proposed architecture separates the physical failure sequence into classification and regression tasks. The Stage-1 classifier defines the penetration boundary and the Stage-2 regressor predicts continuous responses only within the relevant regime. This physics-informed decomposition improves the predictive stability and provides practical guidance for process optimization and material selection.

MATERIALS AND METHODS

The methodological workflow consisted of four connected stages. The first stage generated a broad mechanical-property dataset from 134 heat-treated G33 steel variants. The second stage obtained limited but reliable service-performance data through scaled penetration experiments. The third stage identified the simulation parameters required for finite element penetration modeling and used the validated models to augment the service-performance dataset. The fourth stage used the paired mechanical and service-performance data to train the two-stage prediction framework. This organization avoids treating the experimental, simulation, and learning components as independent procedures and instead presents them as consecutive steps in a unified prediction pipeline.

Raw materials

The G33 ultra-high-strength steel is a low-cost, high-performance steel that can develop either martensitic or bainitic microstructures upon exposure to heat. Its chemical composition is presented in Table 1.

Table 1. Composition range of G33 ultra-high-strength steel (wt%)

GRADE	C	Cr	W	Ni	Si	Mn	Mo	V	Fe
G33	0.33	3.5	4	4	0.8	0.8	0.8	0.4	bal.

The measured phase transition temperatures are as follows: AC3 at 800°C, AC1 at 644°C, Ms at 250°C, and Bs at 360°C. These phase transition points were used as the basis for designing a “three upsetting and three drawing” process, which was implemented for the steel ingots. The specific steps are as follows:

- 1) The initial forging temperature was set at 1,150 °C. The ingot was upset to half of its original height and then drawn back to its original height.
- 2) The ingot was reheated to a temperature of 1,080 °C, upset again to half its height, and then drawn back to the original height.
- 3) The ingot was reheated to 1,050 °C, upset to half its height for the last time, and then forged into rods measuring $\Phi 15 \times 1,000$ mm.

Finally, the rods underwent annealing treatment at 680 °C to effectively relieve the internal stresses induced by the forging process.

A comprehensive range of G33 microstructures was captured for the training dataset by designing heat-treatment schedules that encompass the major bainitic and martensitic transformation pathways. Consequently, we selected specific combinations of the temperature and holding time. Adjustment of the cooling rate and tempering temperature enabled systematic control of the microstructural morphology and distribution, along with the size and dispersion of the precipitated carbides. These microstructural changes strongly influence the toughness, hardness, corrosion resistance, and overall mechanical response of the steel.

Bainitic ultra-high-strength steel was produced via a newly designed two-step heat treatment route consisting of austenitization and isothermal quenching, the latter of which was performed in a salt bath containing 50 wt.% of NaNO₃ and KNO₃. Austenitization was accomplished by increasing the temperature in the range from 900 to 1100°C in increments of 100°C. Because the temperature and holding time of isothermal quenching strongly affect the resulting microstructure, upper bainite was targeted at 345 and 355 °C with a holding time of 30 h, whereas lower bainite was

targeted at 245 and 255 °C with holding times of 10, 20, and 30 h. The steel specimen was cooled in oil in the final stage to reduce quenching stress and distortion. This bainitic route involved six key process parameters and ten procedural variants.

Martensitic ultra-high-strength steel was produced by adopting a heat-treatment route with up to four stages— austenitization, quenching, cryogenic treatment, and tempering. Austenitization was conducted from 700 to 1,100 °C in increments of 50 °C to systematically examine its effect on the microstructural evolution. Water, oil, and air-cooling were used to compare the different quenching conditions. Some schedules also included cryogenic treatment at -73 °C for 1 h to evaluate the effect thereof on the phase morphology and distribution. Tempering was performed over low- (150-200 °C), medium- (200-400 °C), and high-temperature (400-700 °C) ranges with holding times of 2, 4, and 5 h, respectively. Some routes included double tempering to broaden the range of tempering strategies and resulting microstructures. Overall, the martensitic route involved as many as 12 key process parameters and 115 different processing schedules. In addition, nine conventional annealing treatments commonly used for other metallic materials were included for comparison with the pearlitic structures obtained under these conditions.

In total, 134 heat treatment schedules were designed and implemented, which yielded nearly 3 t of test material. Details of the heat-treatment design and the expected primary microstructures are provided in Table S1.

Mechanical property dataset derived from experiments

The mechanical properties that were used to construct the training dataset were acquired directly through experimental testing and comprise 13 basic mechanical properties. The specific parameters are detailed in Table S2.

(1) Quasi-static compression and tensile tests were performed at room temperature.

Quasi-static compression and tensile tests were performed on the 134 steel variants using an INSTRON 5985 universal testing machine. Testing adhered to GB/T 7314-2017 and GB/T 228.1-2010 standards at a strain rate of $1 \times 10^{-3} \text{ s}^{-1}$. Compression specimens measured $\Phi 6 \text{ mm} \times 9 \text{ mm}$, and tensile specimens had a gauge section of $\Phi 5 \text{ mm} \times 30 \text{ mm}$. Each test was repeated at least three times to obtain quasi-static stress-

strain curves at room temperature.

(2) Dynamic compression and tensile tests at room temperature

Dynamic compression and tensile tests were conducted using split Hopkinson pressure and tension bar systems in compliance with the GJB 8374-2015 and GB/T 34108-2017 standards. The dynamic compression tests were conducted with strain rates of 3000 and 5000 s^{-1} , using samples sized $\Phi 5 \text{ mm} \times 5 \text{ mm}$. The dynamic tensile tests were carried out at a strain rate of 2000 s^{-1} , with sample gauge lengths of $\Phi 2 \text{ mm} \times 5 \text{ mm}$. Each test was repeated at least three times to obtain the stress-strain curves for room-temperature dynamic compression and tension.

(3) Vickers hardness tests

The Vickers hardness values of the 134 steel variants were measured using a Wolpert 450SVD tester in the same laboratory. These tests were conducted under a 5 kg load, following the standard GB/T 4340.1-2009. Each material was tested 10 times, and the average Vickers hardness value was used as the final result.

In total, we standardized and collected 1,072 stress-strain curves across various loading conditions. The tests produced 1,742 measurements of the mechanical properties of G33 steel under different heat treatment conditions. These measurements were then visualized, analyzed, and used to construct the dataset. As shown in Fig. 1, the resulting dataset spans a broad numerical range, shows a well-distributed variation, and has a high overall quality. These mechanical property measurements formed the input feature space for subsequent service-performance prediction.

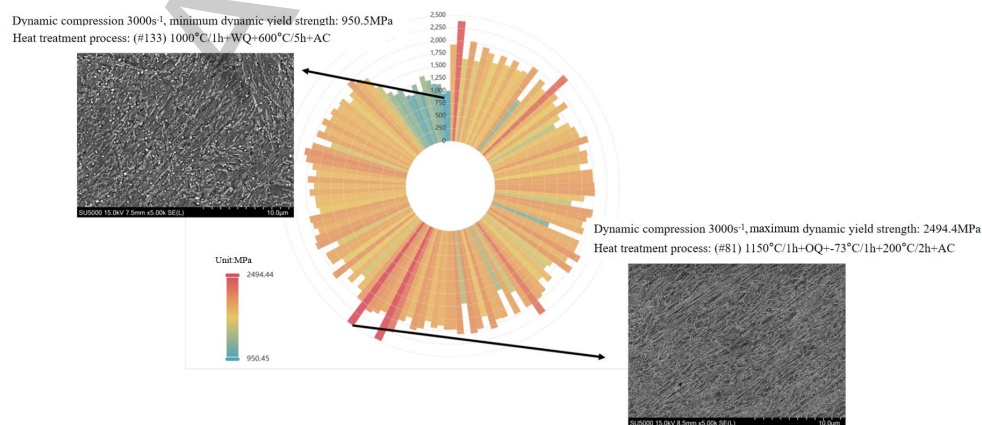


Fig. 1. G33 dataset overview: radial map of dynamic yield strength (3,000 s^{-1}) and

SEMs of the lowest and highest specimens

Service performance dataset generated via high-efficiency simulations

After establishing the mechanical property dataset, the next step was to obtain the corresponding service-performance labels. Because direct penetration testing for all 134 steel variants would be prohibitively expensive, a combined experimental-simulation strategy was adopted. G33 ultra-high-strength steel is primarily used in supersonic kinetic-energy penetrators operating at Mach 2-3; therefore, its service-performance evaluation is centered on penetration efficiency. For deep-penetration applications, two criteria are particularly important: whether the projectile maintains structural integrity after impact and whether it can retain sufficient penetration capability to reach the specified target depth. The essential service-performance parameters used for these evaluations are listed in Table S3.

Scaled penetration experiment using simulated projectiles

The penetration performance of G33 steel was evaluated cost-effectively by performing scaled projectile penetration tests, considering that scaled models can reproduce the key penetration dynamics of actual projectiles at significantly lower costs. These tests also allow repeated testing under controlled conditions, which accelerates service data collection and supports the rapid optimization of both the structure and material.

Among the 134 steel variants, 30 representative samples were selected to cover a broad range of heat-treatment routes and microstructural states. For each category, at least one subgroup was selected to highlight steels with distinctly different performance characteristics to provide a comprehensive evaluation of the behavior of G33 steel under high-speed impact conditions. High-speed photographs of the projectile penetration process are presented in Fig. 2(a), where each sample underwent a minimum of three tests at different penetration speeds. A total of 95 penetration tests were completed. Fig. 2(b) shows a selection of recovered targets and scaled simulated projectiles to illustrate the experimental outcomes.

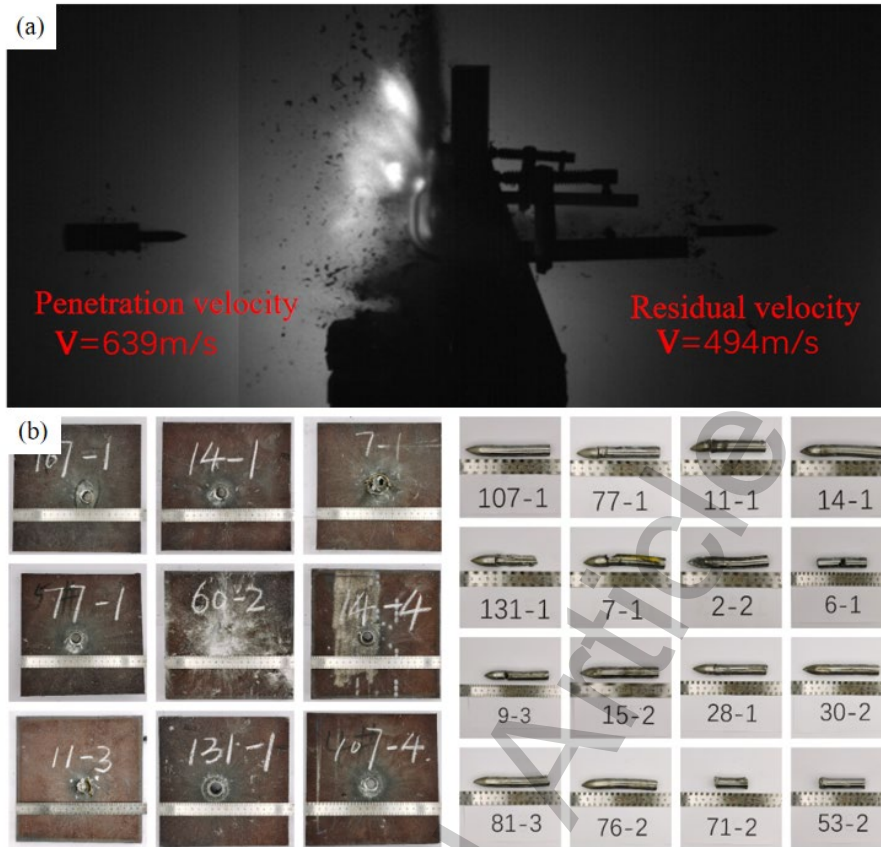


Fig. 2. (a) High-speed camera images; (b) Target plates and scaled projectile samples.

(1) Scaled simulated projectile and target

An ogive-nosed scaled projectile with dimensions of 200 mm × 200 mm × 20 mm was used to impact the naval steel target plates.

(2) Sub-caliber Launch Platform

A 30-37 caliber smoothbore cannon served as the launch platform for the scaled simulated projectiles, as illustrated in Fig. S1(a).

(3) Velocity Measuring Device

In this experiment, the firing distance was set to 3 m and the firing angle was set to 0° to the normal. The initial velocity was determined using a foil interrupt target positioned 1 m from the gun muzzle, as depicted in Fig. S1(b). Additionally, a high-speed camera was employed to validate the launch velocity of the projectile and document the interaction between the projectile and the target, including the post-penetration posture and velocity of the projectile, as shown in Fig. S1(c).

(4) Target frame and projectile recovery device

The steel plate was secured using F-type clamps to ensure that the clamping width around the perimeter did not exceed 20 mm. Rubber pads were applied to the front and back faces of the clamped sections for cushioning, as shown in Fig. S1(d). To retrieve the projectile and any resulting post-penetration fragments, a recovery mat was strategically placed on the after-effect target stand, situated 50 mm behind the steel target, as shown in Fig. S1(e).

A schematic diagram of the scaled projectile penetration test is shown in Fig. S2.

Efficient acquisition method for penetration simulation parameters

The scaled penetration experiments provided reliable reference data but were insufficient in number for robust machine-learning training. Therefore, finite element simulations were introduced to expand the service-performance dataset, provided that the simulation parameters could be accurately identified. Numerical simulations are an effective tool for augmenting the service performance data. Although the scaled penetration tests provided reliable experimental data, most of the service-performance data used in this study were generated by simulations. Because the validity of these results depends on the accuracy of the simulation parameters, an efficient method is required to accurately compute these parameters for the different G33 microstructures. The finite element method (FEM) is widely used in engineering to solve boundary value problems and analyze the response of complex physical systems under service conditions. LS-DYNA is a widely used finite element package that includes models of approximately 300 materials and 16 equations of state. Once reliable simulation parameters are obtained, high-performance computing can be used to lower the experimental costs, shorten the computation time, and support the selection of materials.

Fig. 3 details the parameter acquisition process for penetration simulations. By incorporating these parameters into the models and utilizing large-scale parallel computing, this approach shifts the acquisition of service performance data from costly experimental testing to efficient numerical simulation. This innovative approach, which requires data from only a limited set of physical tests to rapidly compute the service performance parameters for G33 ultra-high-strength steel, substantially augments the sample size of the service performance dataset. Such enhancement significantly

bolsters the accuracy of predictions made by machine learning models.

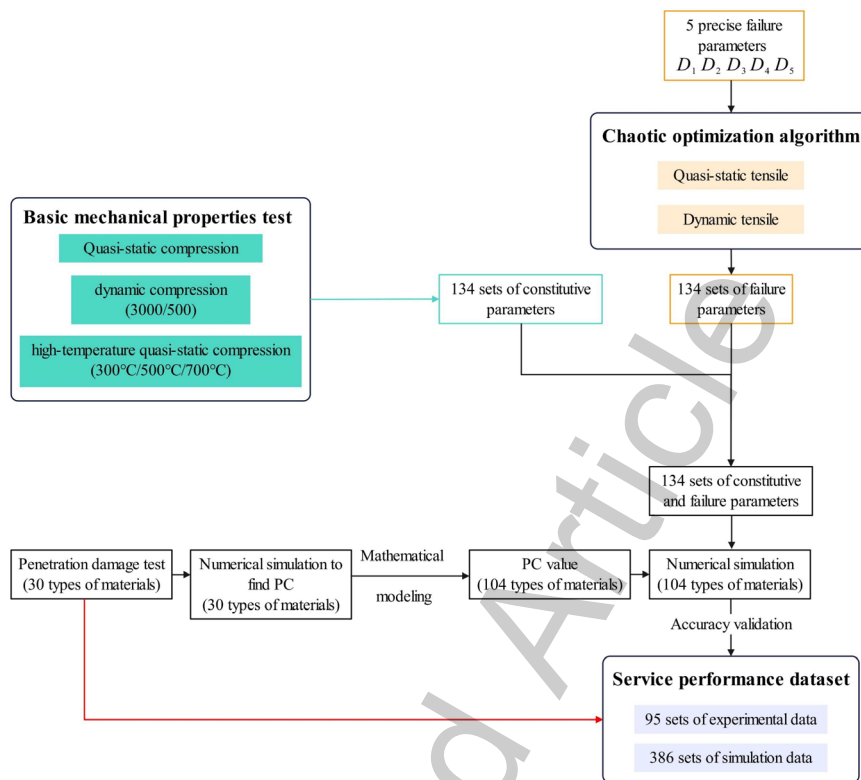


Fig. 3. Flowchart of the parameter acquisition and optimization method for numerical simulation of penetration tests.

The JC constitutive and failure model is widely used in impact and dynamic loading analyses because this model accounts for strain hardening, strain rate sensitivity, and thermal softening. Accurately optimized parameters are necessary to improve the fidelity of the penetration simulations.

To ensure that the simulations accurately captured the behavior of the scaled projectiles penetrating the steel targets, we focused on the deflection of the projectile. A full-scale simulation model was built to match the experimental dimensions by defining the initial velocity using the `*INITIAL_VELOCITY_GENERATION` parameters. Both the projectile and the steel target were modeled using the JC constitutive and failure equations (`*MAT_JOHNSON_COOK`). The target JC parameters derived from experimental fitting are detailed in Table 2. An option to control hourglassing (`*CONTROL_HOURGLASS`) was included to prevent the zero-energy modes

associated with single-point integration. The contact between the projectile and steel target was defined as the eroding surface-to-surface contact (*CONTACT_ERODING_SURFACE_TO_SURFACE). Fixed constraints (*BOUNDARY-SPC_SET) were applied to the contact area between the steel target and target frame to simulate the support provided by the frame.

Table 2. Johnson-Cook constitutive and failure equation parameters for marine steel

Constitutive Parameters	A	B	n	C	m
	0.0068	0.0055	0.2000	0.0200	1.0000
Failure Parameters	D_1	D_2	D_3	D_4	D_5
	0.1580	0.2100	3.9700	0.0010	1.0000

In addition to the constitutive and failure parameters, the penetration simulation requires auxiliary parameters. Notably, the PC value (keyword: *MAT_JOHNSON_COOK_PC: Failure stress or pressure cutoff) is an integral failure criterion. Without an explicit physical interpretation, this parameter cannot be calibrated directly through experimentation. In the simulation model, once the first principal stress within an element reaches a predefined threshold, it is eliminated automatically. This mechanism, in concert with the JC failure parameters, effectively dictates the failure dynamics of the material.

Overall, the penetration simulation model required 11 parameters, as summarized in Table 3.

Table 3. Parameters of the numerical simulation model for penetration tests

Category	Required Parameters				
JC Constitutive Equation	A	B	n	C	m
JC Failure Equation	D_1	D_2	D_3	D_4	D_5
Other Parameters	Supporting Failure Criterion PC Value				

The efficient determination of the parameters listed in Table 3 is described below.

(1) The JC constitutive equation is^[23]:

$$\sigma = (A + B\varepsilon^n)(1 + C\ln\dot{\varepsilon}^n)(1 - (T^*)^m), \quad (1)$$

where ε denotes the equivalent plastic strain, $\dot{\varepsilon}^* = \dot{\varepsilon}/\dot{\varepsilon}_0$ is the dimensionless plastic strain rate, and $\dot{\varepsilon}$ represents the strain rate. The reference strain rate is set as $\dot{\varepsilon}_0 = 0.001/s$ in this study. $T^* = (T - T_r)/(T_m - T_r)$ signifies the dimensionless temperature in Kelvin (K), T is the absolute temperature, T_r is the room temperature at 298 K, and T_m is the melting point of the ultra-high-strength steel. The three terms in the equation correspond to strain hardening, strain-rate hardening, and thermal softening, respectively. Parameters A , B , n , C , and m are the material constitutive parameters that require fitting. These five parameters were determined using a clustering global optimization algorithm previously developed by our research group^[24].

(2) Understanding the behavior of a material under complex stress states is fundamental to the design of new structural materials. Macroscopic failure results from damage accumulation until a critical threshold is reached. This damage is associated with the microstructural changes induced by temperature, loading, and other service conditions, which initiate microdefects, cause them to grow and coalesce, and eventually form fractures. Because ductile fracture in metallic materials is strongly influenced by the stress triaxiality, strain rate, and temperature, an appropriate failure equation is required to describe the damage behavior of ultra-high-strength steel during loading.

The form of the JC failure equation is^[23]:

$$\varepsilon_f = [D_1 + D_2 \exp(D_3\sigma^*) (1 + D_4 \ln\dot{\varepsilon}^*) (1 + D_5 T^*)] \quad (2)$$

In the equation, ε_f represents the failure strain, σ^* denotes the stress triaxiality, $\dot{\varepsilon}^* = \dot{\varepsilon}/\dot{\varepsilon}_0$ is the dimensionless plastic strain rate, and $\dot{\varepsilon}$ represents the experimental strain rate. In this study, the reference strain rate is set at $\dot{\varepsilon}_0 = 0.001/s$. $T^* = (T - T_f)/(T_m - T_f)$ indicates the dimensionless temperature in Kelvin (K), T is the temperature, T_f is the reference temperature, taken as room temperature (298 K) in this study, and T_m is the melting point of the ultra-high-strength steel. Parameters

$D_1 - D_3$ were derived by fitting the diameters of the fracture surfaces of the tensile test specimens with varying notch radii. Parameters D_4 and D_5 were derived by fitting the fracture surface diameters from the dynamic tensile specimens across different strain rates and from the high-temperature quasi-static specimens across various temperatures.

Traditional approaches for determining JC failure parameters require extensive empirical testing and often ignore parameter interdependencies. This disjointed fitting process is inefficient and rarely yields globally optimal solutions. By leveraging insights into the parameter influence patterns and utilizing global optimization algorithms, a novel methodology was developed to obtain the JC failure parameters from quasi-static and dynamic tensile tests. This approach enables accurate and relatively high-throughput parameter identification to build the service performance dataset.

The chaos optimization algorithm leverages the ergodicity and the sensitivity of chaotic systems to the initial conditions to enhance the search diversity. Unlike conventional algorithms, this approach effectively prevents premature convergence to local optima (a common complication in conventional optimization algorithms) making it highly suitable for complex multidimensional problems. Because it can search for multiple variables simultaneously, it is well-suited to the coupled multiparameter inversion problem addressed here.

Unlike traditional metaheuristic methods such as genetic algorithms (GA) and particle swarm optimization (PSO), which may converge prematurely in highly nonconvex multidimensional parameter spaces, the chaos optimization algorithm exploits the ergodicity and pseudo-randomness of chaotic maps. This feature renders it suitable for the inversion of JC parameters in the present study.

According to chaos theory, seemingly random behaviors can arise in deterministic systems. Although chaotic trajectories appear disordered, they follow deterministic rules and can provide broad, nonrepetitive coverage of a bounded interval after sufficient iteration. Chaotic variables can be generated using several mappings, including logistic, cubic, and infinite folding maps. Among these, the infinite folding

map provides a relatively balanced distribution with fewer iterations, which helps accelerate the convergence in the present optimization procedure. Therefore, it was selected for the present study.

The logistic equation is shown in Equation (3), with the initial value μ in the range (0, 1). When $v = 4$, the system is in a state of chaos^[25].

$$\mu_{i+1} = v\mu_i(1 - \mu_i), \mu \in (0, 1), \mu \neq 0.25, 0.5, 0.75 \quad (3)$$

The cubic mapping equation is given in Equation (4). Within the interval (-1, 1), chaos occurs when the initial value is not zero. After multiple iterations, the generated points were randomly distributed, and even a slight difference in the initial value could cause significant changes in the output^[26].

$$\mu_{i+1} = 4(\mu_i)^3 - 3\mu_i, \mu \in (-1, 1), \mu \neq 0 \quad (4)$$

The infinite folding mapping equation is presented in Equation (5). Within the interval (-1, 1), chaos occurs when the initial value is not zero. After multiple iterations, the generated points are randomly distributed, thereby facilitating traversal of the entire system space^[27].

$$\mu_{i+1} = \sin\left(\frac{2}{\mu_i}\right), \mu \in (-1, 1), \mu \neq 0 \quad (5)$$

Chaos optimization linearly maps chaotic variables onto the search space of decision variables, using the resulting trajectories for global optimization. The algorithm explores candidate solutions through a chaotic search and progressively narrows the search interval to accelerate convergence. Because chaotic motion combines randomness with ergodicity, this procedure improves the chance of identifying a near-global or global optimum.

The simulations were performed using the actual dimensions of the experimental setup. The details are presented in Fig. S3.

In this study, specimen #121 of the G33 ultra-high-strength steel was examined with designated ranges for the JC failure parameters $D_1 - D_5$. Numerical simulations of the quasi-static and dynamic tensile tests were performed to ascertain the impact of these parameters on the simulation results. Detailed analyses of the fracture elongation rates for both testing modalities were conducted, and the results are shown in Fig. 4. The results indicated that increments in the JC parameters D_1 and D_2 , along with a decrease in D_3 , significantly affected the fracture elongation rates observed in the numerical simulations, leading to continuous linear variations in the outcomes. This reveals the critical influence of these parameters on the material performance. In contrast, the modulation of parameters D_4 and D_5 has minimal impact on the experimental results, highlighting their limited effect on the material properties.

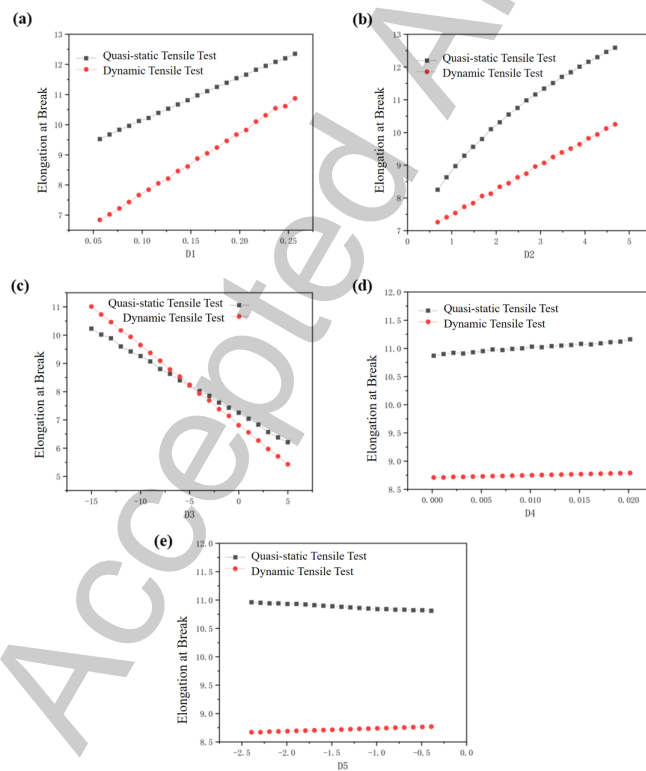


Fig. 4. Influence of JC failure parameters $D_1 \sim D_5$ on numerical simulation results.

Overall, the numerical simulations of the quasi-static and dynamic tensile tests demonstrated that parameters $D_1 - D_3$ had a substantial effect on the results, whereas the influences of D_4 and D_5 were marginal. This indicated that the simulation models for these tests can be utilized for precisely tuning and verifying parameters $D_1 - D_3$.

Parameters D_4 and D_5 may be fixed within a certain range to reduce the complexity of the model while ensuring the reliability of the simulation outcomes.

The fracture failure behavior of G33 ultra-high-strength steel under quasi-static tensile testing was systematically analyzed to determine the optimal ranges for the JC failure parameters $D_1 - D_3$, as well as specific values for D_4 and D_5 . The fracture elongation rates were thoroughly examined, and the results are shown in Fig. 5. The dataset was divided into five intervals, and one representative material was selected from each interval for fitting, resulting in five samples. Materials whose fracture elongation was close to the median value of each interval were selected, while differences in microstructure and heat-treatment history were also considered to ensure representativeness. The fitted JC failure parameters are listed in Table 4.

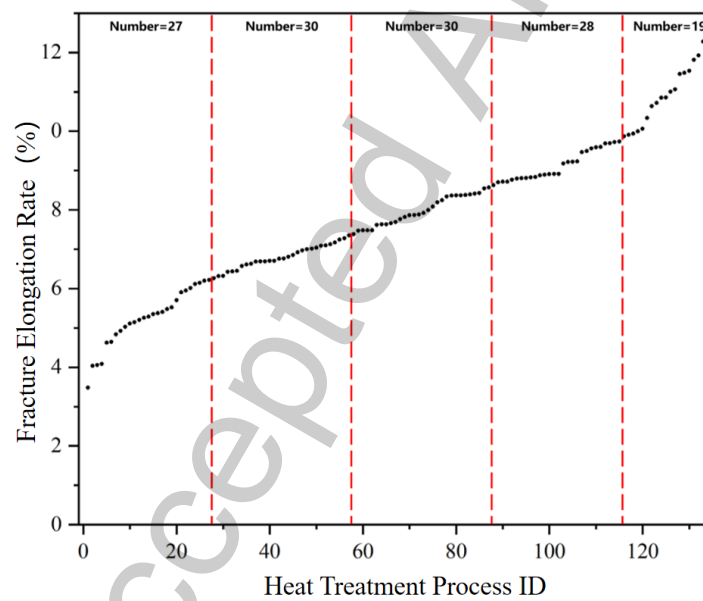


Fig. 5. Statistical chart of fracture elongation in quasi-static tensile tests of ultra-high-strength steel.

Table 4. Statistical table of JC failure equation parameters for 5 types of ultra-high-strength steel

ID	D_1	D_2	D_3	D_4	D_5
#25	0.0422	0.0736	-2.1799	-0.0185	0.5472
#80	0.0357	2.4998	-4.3184	-0.0068	-0.7419
#93	0.2073	1.6284	-2.8741	-0.0182	0.1258

ID	D_1	D_2	D_3	D_4	D_5
#109	0.1139	3.1154	-5.6164	-0.0158	0.6378
#121	0.1569	2.6815	-5.4423	0.0062	-1.3978

Within each interval, the fitted values for parameters $D_1 - D_3$ were expanded both upward and downward to create numerical ranges that served as input domains for the chaotic optimization algorithm. Parameters D_4 and D_5 were assigned constant values common to all ultra-high-strength steel samples within these ranges. To precisely optimize parameters $D_1 - D_3$, simulation models were constructed for both the split Hopkinson tension bar (SHTB) test and the quasi-static tensile test. An infinite folding chaotic map is then used to generate candidate parameter sets within the prescribed ranges for global optimization. The optimization procedure is illustrated in Fig. 6 and described below.

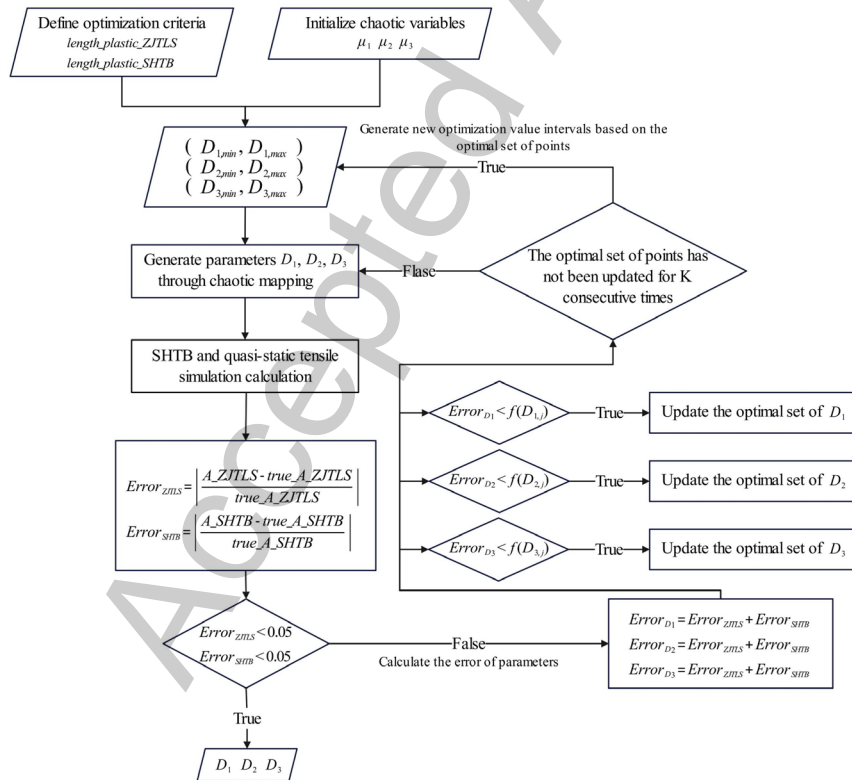


Fig. 6. Chaotic optimization path for JC failure equation parameters.

The model optimization procedure is summarized as follows:

- ① Initialization of Chaotic Variables and Setting Optimization Goals: Experimental results are used as target values for simulation calculations. Three distinct nonzero

numbers, μ_1 , μ_2 , and μ_3 , within the range of (-1, 1) are selected as initial values for the chaotic variables.

② Determination of Optimization Intervals for Parameters $D_1 - D_3$: Incorporate the optimization interval (-1, 1) and adjust its size according to practical considerations to enhance the computational efficiency.

③ Mapping Chaotic Variables to Parameter Values: Using Equation (6), the chaotic variables are mapped into the optimization intervals to generate the parameters $D_1 - D_3$, which are then input into the simulation model for computation^[28].

$$x = \frac{b + a}{2} + \frac{b - a}{2} \times \mu \quad (6)$$

④ Extraction of Simulation Results and Calculation of Simulation Errors^[29]: The error in the quasi-static tensile simulation is calculated as shown in Equation (7), where A_{ZJTLS} represents the fracture elongation rate from the quasi-static tensile simulation, and $true_{A_{ZJTLS}}$ is the fracture elongation rate obtained experimentally. The error in the SHTB simulation is outlined in Equation (8), where A_{SHTB} denotes the fracture elongation rate from the SHTB simulation, and $true_{A_{SHTB}}$ represents the experimentally obtained SHTB fracture elongation rate.

$$Error_{ZJTLS} = \left| \frac{A_{ZJTLS} - true_{A_{ZJTLS}}}{true_{A_{ZJTLS}}} \right| \quad (7)$$

$$Error_{SHTB} = \left| \frac{A_{SHTB} - true_{A_{SHTB}}}{true_{A_{SHTB}}} \right| \quad (8)$$

⑤ Calculation of Errors for Parameters $D_1 - D_3$ ^[29]: Given the significant impact of parameters $D_1 - D_3$ on both models, their error is computed as the sum of errors from the two simulation models, as outlined in Equation (9).

$$Error_{D_{1-3}} = Error_{ZJTLS} + Error_{SHTB} \quad (9)$$

⑥ Establishment of the Initial Optimal Solution Set: The number of solutions in the initial optimal set is defined as N , with the first N points generated by the chaotic variables serving as the initial optimal solutions. Let $D_{1,i}$ denote the values of D_1 after the i th iteration. If the error for $D_{1,i}$ ($Error_{D_1}$) is less than the maximum error in the optimal set, $f(D_{1,j})$, where $D_{1,j}$ corresponds to the point with the highest error, then $D_{1,j}$ is replaced by $D_{1,i}$ in the optimal set. Similarly, the optimal solution sets for D_2 and D_3 are updated according to the same principle.

⑦ Iteration and Convergence Criteria: A parameter K was specified. If the optimal solution set for a given parameter remains unchanged for K consecutive iterations, the bounds of that set are adopted as the new optimization interval for the next cycle, and the procedure returns to Step 2.

⑧ Termination of Optimization: The optimization process concludes when the errors for all parameters simultaneously meet the predefined target errors, that is, when $Error_{D_1}$, $Error_{D_2}$, and $Error_{D_3}$ all satisfy the error criteria, and the optimized results are output. If the criteria were still not satisfied after several iterations, the parameter set with the smallest error in the optimal solution set was considered as the final result.

By combining experimental testing, numerical simulations, and parameter optimization, the JC constitutive and failure parameters were efficiently fitted for all 134 G33 steel variants.

(3) Validation of numerical simulation parameter accuracy in penetration testing.

To verify the accuracy of the service performance data derived from the simulation, one ultra-high-strength steel sample was randomly selected from each of the three groups: samples lying on the fitted surface and the outliers above and below it. The samples were subjected to scaled projectile penetration simulations. As shown in Table 5, all the simulation errors were below 10%, thereby satisfying the dataset accuracy requirement. Fig. S4 compares the recovered projectile morphology after the penetration test at 727 m/s with the corresponding simulation results for G33 sample #128. The projectile

shapes were consistent, and the residual velocity error after target penetration was only 3.6%. These results support the use of high-throughput simulations to generate service performance data for subsequent machine learning analysis.

Table 5. Comparison of target test results and numerical simulation results for the critical projectile fracture penetration speed of G33 ultra-high-strength steel

ID	Heat Treatment Process	Target	Numerical	Error Rate (%)
		Test Results (m/s)	Simulation Results (m/s)	
#4 0	1100°C/1 h+OQ+-73°C/1 h+560°C/5 h+AC	728	680	6.6
#8 3	1050°C/1 h+OQ+-73°C/1 h+200°C/4 h+AC	830	915	9.3
#1 28	1000°C/1 h+WQ+250°C/5 h+AC	735	680	7.5

This study established an efficient method for determining the numerical simulation parameters required for penetration analysis. Through a combined experimental validation and high-fidelity simulation, a paired dataset containing 483 sets of mechanical and service performance data was constructed (95 experimental service performance samples and 388 additional high-fidelity simulation samples). The dataset includes five target metrics: scaled projectile penetration velocity, penetration occurrence, post-penetration projectile integrity, residual velocity after perforation, and critical velocity for projectile fragmentation. Our strategy substantially reduced the experimental cost while improving the data acquisition efficiency, thereby providing a solid basis for the predictive modeling of the relationship between the mechanical properties and service performance.

RESULTS AND DISCUSSION

Overview of the methodology

Based on the paired dataset generated in Section 2, a two-stage machine-learning framework was constructed to map conventional mechanical properties to ballistic

service responses. The overall workflow of this framework is illustrated in Fig. 7. The framework was designed according to the physical sequence of the penetration process. In the first stage, a random forest classifier determined whether penetration occurred. For penetrated cases, the samples were passed to the second stage, in which a multilayer perceptron regression was used to predict the residual velocity and critical fragmentation velocity, while a separate random forest classifier evaluated post-penetration projectile integrity. This staged design prevented the regression model from assigning physically unrealistic residual velocities to non-penetrated cases and improved the consistency between the model outputs and the actual penetration process.

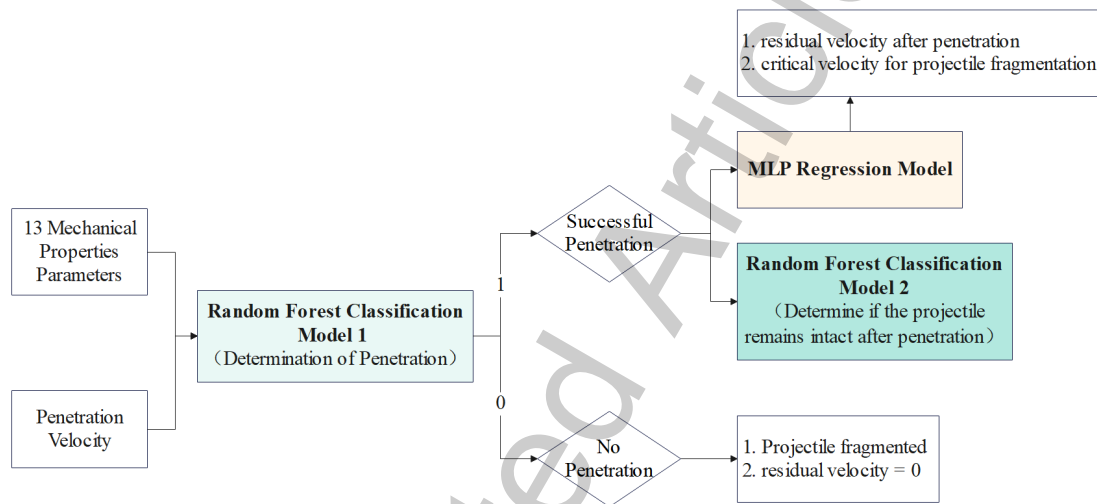


Fig. 7. Flowchart of the two-stage model development for predicting operational performance parameters

Operational performance classification model based on random forest

Random forest classification models were developed to predict two service outcomes: whether penetration occurred and whether the projectile remained intact after penetration. Random forest is an ensemble learning method based on decision trees and is well known for its robustness and predictive accuracy on tabular data. It also provides estimates regarding the importance of features that are valuable for physical interpretations in material engineering. A decision tree consists of root, internal, and leaf nodes. The root node contains all the training data, each internal node splits the data according to a selected feature, and the leaf nodes represent the final categories.

The hyperparameters of the random forest models were optimized using GridSearchCV, which exhaustively searches for a predefined parameter grid and evaluates each

combination through cross-validation. The parameter grid used in this study ('param_grid') included the major random forest hyperparameters and their candidate values.

The specific grid parameters of the developed random forest classification model are listed in Table S4.

Operational performance regression model based on MLP

The multilayer perceptron (MLP) is a feedforward artificial neural network composed of an input layer, one or more hidden layers, and an output layer. As each layer is fully connected to the next layer, the MLP can learn nonlinear relationships and is suitable for complex regression tasks. In this study, a relatively shallow MLP was used to capture the nonlinear mapping between the mechanical properties and ballistic performance while limiting the risk of overfitting.

To predict the continuous service performance metrics, namely the post-penetration residual velocity and critical fragmentation velocity, we developed a three-layer MLP regression model. The input layer contained 128 neurons, the hidden layer contained 64 neurons, and the output layer contained a single neuron that produced a predicted value. The detailed model configurations are listed in Table S5.

The model was trained with the Adam optimizer using an initial learning rate of 10^{-3} and a decay of 10^{-5} . This setting enabled stable convergence during training. All calculations were performed using Python 3.

Comparison with baseline models and ablation analysis

The benefits of the proposed architecture were assessed by comparing its performance with that of a conventional single-stage baseline model (for example, unified MLP). As depicted in Figs. S5 and S6, the single-stage model proved inherently deficient in that it was unable to map the abrupt discontinuity at the ballistic limit, and often erroneously predicted positive residual velocities for unpenetrated targets. In contrast, the two-stage RF + MLP framework imposed a physically meaningful classification boundary before regression, eliminated these zero-boundary anomalies, and reduced the mean absolute error (MAE) from 33.7 to 30.4 m/s.

Ablation analysis further demonstrated that each module contributed to the final performance. Removing the feature selection step introduced redundant dimensionality and weakened generalization, whereas omitting the chaos-based optimization compromised the quality of the simulation-generated data because the parameter search became more prone to converging to local optima. These results indicate that an integrated framework is necessary for accurate and physically consistent ballistic prediction.

Impact of data augmentation and generalization analysis

A key limitation of data-driven terminal ballistics research is the scarcity of experimental service performance data. In this study, the reliance on only 95 physical firing tests creates a serious risk of overfitting, in which the model learns the training samples but fails to generalize them to new material states.

The role of chaos-optimized finite element data augmentation was therefore evaluated by constructing a learning curve (Fig. S7) to track the training and cross-validation performances as the dataset became larger. The addition of increasing numbers of high-fidelity simulation samples steadily increased the cross-validation accuracy. The curve indicated that the model generalization stabilized only after the dataset exceeded 125 samples.

The evaluation with the learning curve indicates that the high predictive accuracy of the proposed framework is not simply a consequence of fitting a small dataset. Rather, it arises from the combination of physics-informed high-throughput simulation augmentation, which expands the dataset to 483 reliable samples, and a two-stage learning architecture that simplifies the prediction task and improves generalization.

Error analysis, validation, and model uncertainty

Stratified 10-fold cross-validation enabled the generalization to be rigorously assessed. Stratification preserved the class imbalance between penetration and non-penetration cases across all folds, thus reducing the evaluation bias toward the majority class.

The predictive reliability was further examined using a classification confusion matrix

(Fig. S8) and a regression residual plot (Fig. S9). The confusion matrix showed that the Stage-1 random forest accurately identifies the ballistic limit boundary. The residual plot for the Stage-2 MLP revealed that the residual velocity errors were approximately symmetric about zero without any obvious systematic bias.

Despite the high overall accuracy, analysis of the worst predicted cases provided important insights into the model uncertainty. The highest prediction variances were clustered exactly at the threshold of the ballistic limit (V_{50}). From a materials science perspective, the terminal ballistic response at this critical boundary is highly stochastic. The transition between partial embedment and complete perforation is highly sensitive to random microstructural inhomogeneities, such as the localized distribution of microvoids or inclusions. These microscopic defects introduced inherent aleatoric uncertainties into the dynamic fracturing process. Considering that the current model accepts deterministic macroscopic mechanical properties as its input, the prediction uncertainty increases near this transition point. Recognizing this stochastic boundary is important for the practical use of data-driven models in armor design.

Operational performance prediction based on the entire dataset

The input and output data were standardized, and a 10-fold cross-validation was used to divide the dataset into training and testing subsets. This was accomplished by randomly splitting the full dataset into ten subsets, with each iteration using one subset as the test set and the remaining nine subsets for training. This procedure yielded ten models, and the performance was evaluated based on the average accuracy across ten folds. The results reported in this section correspond to the full feature model before the feature selection.

The predictive accuracies of the various models on their test sets are detailed in Fig. 8. The classification model for projectile penetration achieved a high accuracy of 98.8% with minimal variability (4.2%), thereby demonstrating robust generalization and stability across data partitions. In contrast, the classification model assessing the integrity of the projectile post-penetration achieved an accuracy of 72.9%, with a substantial variability of 18%, indicating potential dependency and sensitivity to specific datasets, which could constrain the predictive performance. The regressor for the residual velocity after penetration achieved an accuracy of 92.7%, with a variability

of 5.6%, indicating good generalization and stability. Here, variability refers to the range of results obtained from 10-fold cross-validation.

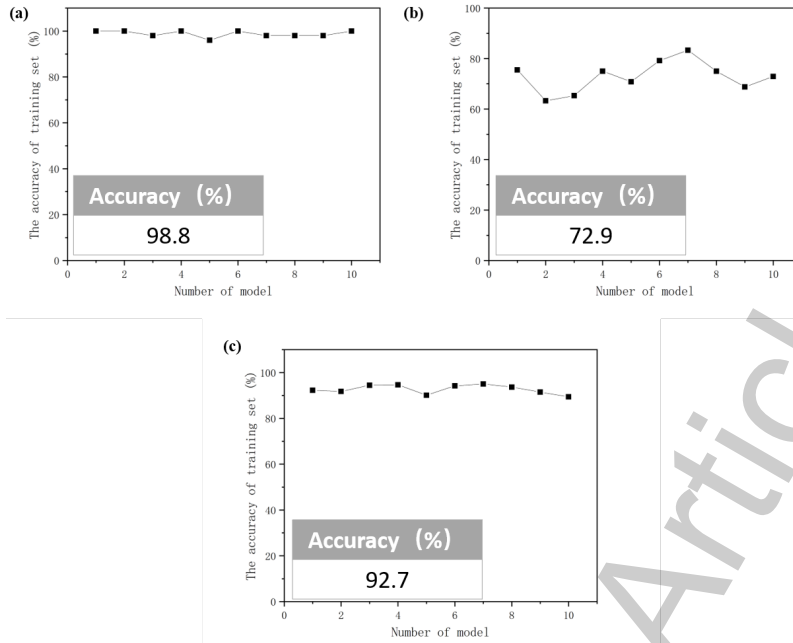


Fig. 8. Accuracy of the test set for the mechanical and operational performance prediction model (full-feature model): (a) Classification model for projectile penetration; (b) Classification model for post-penetration projectile integrity; (c) Regression prediction model for residual velocity after projectile penetration

For the regression tasks, the accuracy was defined as $(1 - \text{MAPE}) \times 100\%$, where MAPE is given by:

$$\text{MAPE} = \frac{1}{n} \sum_{i=1}^n \left| \frac{y_i - \hat{y}_i}{y_i} \right| \quad (10)$$

Here, n represents the total number of samples, y_i is the observed value of the i th sample, and \hat{y}_i is the predicted value of the i th sample.

Operational performance prediction based on parameter selection

The preceding analysis utilized a dataset containing 1,742 values relating to the mechanical properties, and predicted the service performance metrics with high accuracy. However, collecting a large number of mechanical parameters is time-consuming, expensive, and sensitive to experimental variations. In addition, many

parameters were correlated with each other. To reduce redundancy and streamline data collection, the Pearson correlation coefficients were calculated between all feature pairs and used for feature selection.

The equation for calculating the Pearson correlation coefficient is presented in Equation (11)^[30]:

$$r_{xy} = \frac{1}{n-1} \frac{\sum_{i=1}^n (x_i - \bar{x})(y_i - \bar{y})}{S_x S_y} \quad (11)$$

where x_i and y_i denote individual parameter values, whereas \bar{x} and \bar{y} are the means of the respective parameter sets, and S_x and S_y are their standard deviations. The sign of the Pearson correlation coefficient indicates whether the relationship is positive or negative and its magnitude indicates the strength of the correlation. Values closer to 1 or -1 indicate stronger correlations, with positive and negative signs representing direct and inverse relationships, respectively.

Fig. 9 presents the Pearson correlation coefficient matrix for the 13 sets of parameters. In this research, a threshold of 0.9 was established. Any pair of parameters with an absolute correlation coefficient exceeding this value was considered highly redundant, which necessitated the retention of only one parameter from each correlated pair. Based on the analysis depicted in the figure, five parameter sets were removed: the quasi-static tensile strength, quasi-static compressive yield strength, Vickers hardness, dynamic compressive strength at 3,000 s⁻¹, and dynamic compressive strength at 5,000 s⁻¹.

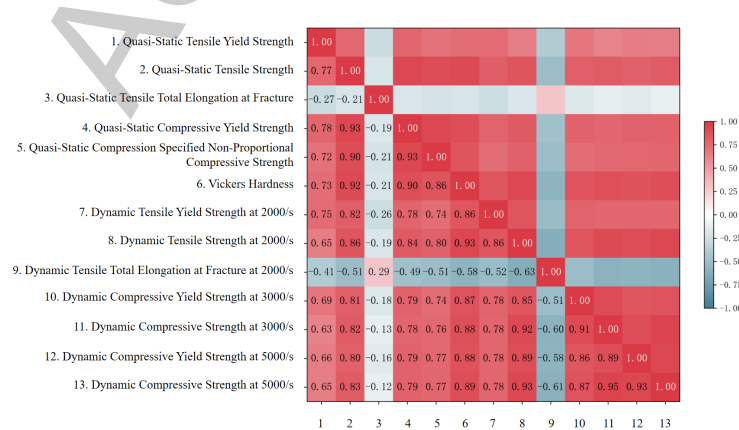


Fig. 9. Pearson correlation coefficient matrix.

After feature selection, eight parameters relating to the mechanical properties together with the penetration velocity were used as inputs to the two-stage model, and the service performance predictions were recalculated using 10-fold cross-validation. The results of the final optimized feature selection model are shown in Fig. 10. The classification model that determined projectile penetration maintained a high accuracy of 98.3% with a variability of 4.2%, demonstrating robust predictive precision. This indicates that the elimination of the five redundant parameters had a minimal impact on the predictive performance of the model, whereas the nine retained parameters sufficiently encapsulated the critical determinants of the model output. The classification model assessing the integrity of the projectile post-penetration improved the output accuracy of the model to 74.8% with a reduced variability of 18%, thereby significantly lowering its sensitivity to specific data subsets. Meanwhile, the regression model predicting the residual velocity of the projectile after penetration enhanced the accuracy of the model output to 92.9% while maintaining a variability of 5.6%. These improvements further bolstered the generalization capabilities of the model.

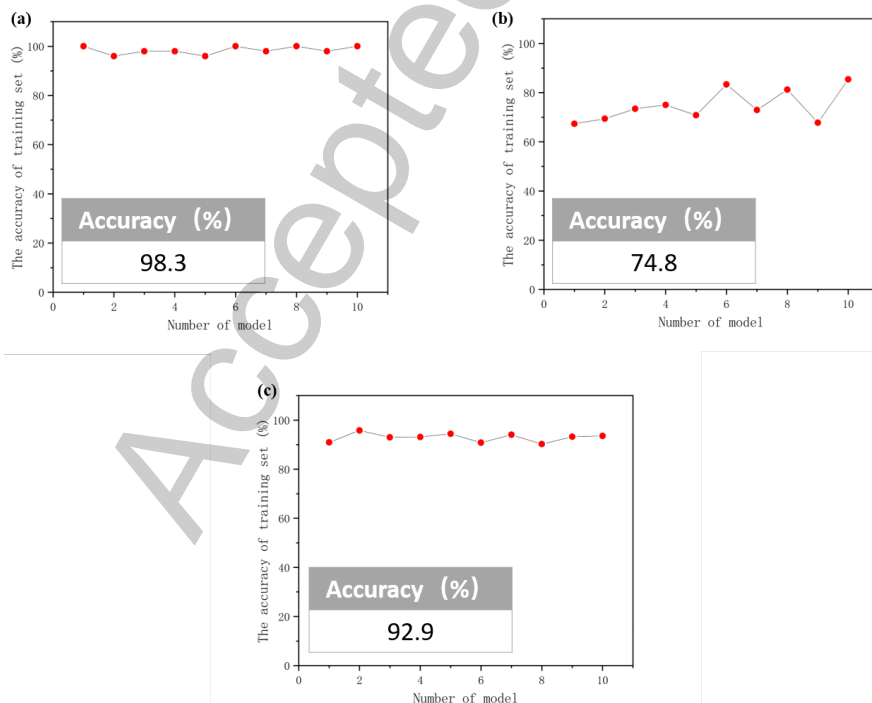


Fig. 10. Predictive accuracy of the test set (final optimized feature-selected model) for the mechanical and operational performance prediction model after feature optimization: (a) Classification model for projectile penetration; (b) Classification

model for post-penetration projectile integrity; (c) Regression prediction model for residual velocity after projectile penetration.

By removing redundant parameters, the input dimensionality was reduced, training became more efficient, and model generalization was improved. This refinement allowed the model to capture the key factors governing the output with fewer parameters, thereby reducing the data collection effort and shortening the prediction process.

However, even after feature reduction, the predicted service performance variables remained relatively scattered, which made a direct comparison among materials less straightforward. Additional statistical processing is still required to efficiently rank the materials. Therefore, we selected the critical projectile fracture penetration velocity, which is defined as the highest penetration velocity at which the projectile remains intact, as a single comparative indicator that directly links the mechanical properties to service performance.

Fig. 11 illustrates the predictive accuracy distribution of the regression model for assessing the critical projectile fracture penetration speed of G33 ultra-high-strength steel. The model achieved an average predictive accuracy of 89.8% with a variability of only 8.9%, demonstrating both high precision and robust stability in predicting critical speeds. The selected experimental data and the corresponding model predictions are presented in Table 6. This model enables the direct estimation of the critical projectile fracture penetration velocity from mechanical property data and thus provides a practical basis for rapid service performance assessment and material optimization.

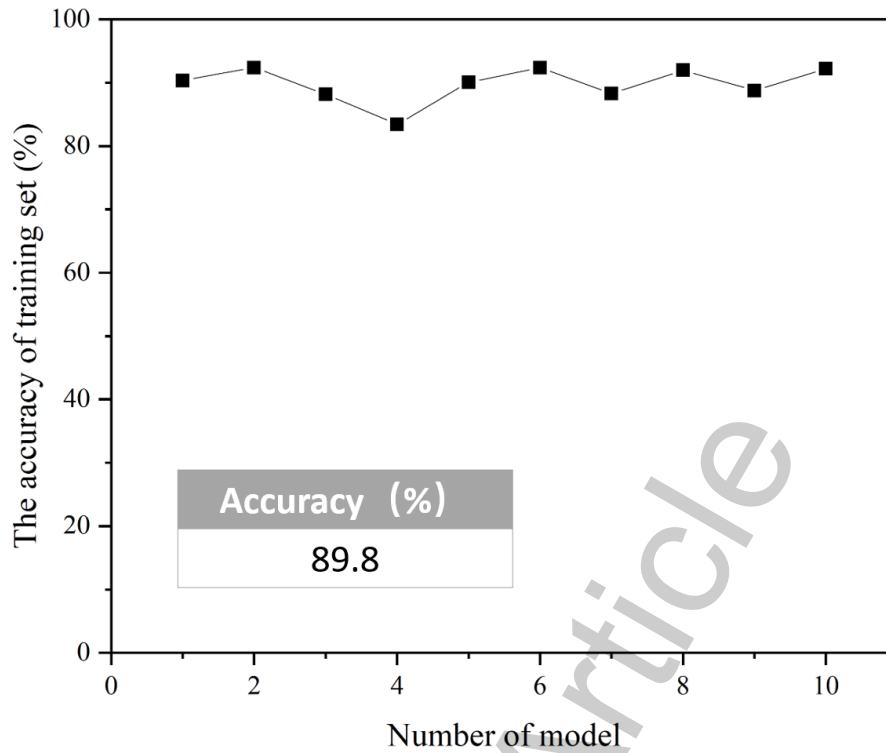


Fig. 11. Distribution of predictive accuracy for the regression model test set of critical projectile fracture penetration velocity (final optimized model) for G33 ultra-high-strength steel.

Table 6. Selected experimental and predicted results for the critical projectile fracture penetration velocity of G33 ultra-high-strength steel

ID	Heat Treatment Process	Experimental Results (m/s)	Predicted Result (m/s)	Error (%)	Rate
#6	900°C/1 h+OQ+400°C/2 h+AC	713	617	13.46	
#5	900°C/1 h+OQ+-73°C/1 h+560°C/2 h+AC	705	732	6.67	
#5	1050°C/15 h+FC	720	708	1.67	
#5	900°C/1 h+FC	795	733	7.80	
#8	1150°C/1 h+OQ+-73°C/2 h+200°C/4	795	723	9.06	

Feature interpretability and physical mechanisms

In materials informatics, model interpretability is essential for guiding material design. Therefore, SHAP analysis was performed on the nine key input features retained after feature selection to examine whether the proposed two-stage framework captured meaningful structure-property relationships. As shown in Fig. S10, the SHAP results indicate that the penetration response is mainly controlled by high-strain-rate mechanical properties, while quasi-static properties and impact velocity play secondary roles. Among all features, Dynamic Tensile Elongation at $2,000 \text{ s}^{-1}$ shows the highest importance, suggesting that dynamic ductility strongly affects plastic energy dissipation and resistance to back-face tearing or spalling under impact loading. Dynamic Compressive Yield Strengths at $5,000$ and $3,000 \text{ s}^{-1}$ are the next most influential features, reflecting their role in resisting localized plastic deformation and delaying adiabatic shear band formation during high-rate compression. In contrast, the lower importance of Impact Velocity and Quasi-Static Tensile Yield Strength further suggests that terminal ballistic performance is governed primarily by dynamic, rather than quasi-static, mechanical responses. These results confirm that the model predictions are physically consistent with established mechanisms of dynamic impact and fracture.

CONCLUSIONS

In summary, this study established a robust two-stage machine-learning framework to rapidly evaluate the performance of extreme service materials from their conventional mechanical properties. This approach effectively overcomes the data scarcity inherent in penetration testing by integrating chaos-based global optimization with high-throughput finite element simulations. The dual-stage architecture minimizes feature redundancy while successfully mapping standard mechanical inputs to complex terminal responses such as penetration occurrence and critical fracture velocity. Validated on G33 ultra-high-strength steel, the model demonstrated high predictive accuracy and consistency. This framework offers a highly transferable and practical strategy for accelerating the design, selection, and performance assessment of advanced materials for extreme-impact environments.

DECLARATIONS

Acknowledgments

The authors acknowledge the use of Google Gemini (Version: Gemini 3.1 Pro, incorporating the Nano Banana image generation model) for the initial conceptualization and foundational layout of the Graphical Abstract. It is important to note that the AI-generated output served only as a base template. The authors subsequently modified the image by integrating authentic experimental scene photographs and specific research data. The authors have rigorously verified the final output and take full responsibility for the scientific accuracy, data integrity, and ethical compliance of the resulting composite image, ensuring it faithfully represents the core findings of this manuscript without any copyright infringement.

Authors' contributions

Writing - original draft preparation, Formal analysis, Investigation, Data curation, Visualization: Qichao Wei.

Writing - original draft preparation, Conceptualization, Methodology, Formal analysis, Data curation, Supervision: Pingluo Zhao.

Writing - original draft preparation, Data curation: Qiang Hao.

Writing - original draft preparation, Formal analysis, Investigation, Data curation, Visualization: Wuguo Chen.

Project administration, Funding acquisition, Supervision: Hongmei Zhang; Yangwei Wang; Xingwang Cheng.

All authors have read and agreed to the published version of the manuscript.

Availability of data and materials

The data supporting the findings of this study are available from the corresponding author upon reasonable request.

Financial support and sponsorship

The work was supported by the National Key Laboratory Foundation of Science and Technology on Materials under Shock and Impact (6142902240301), and the Fundamental Research Funds for the Central Universities.

Conflicts of interest

The authors declare no conflicts of interest.

Ethical approval and consent to participate

Not applicable.

Consent for publication

Not applicable.

Copyright

© The Author(s) 2026.

REFERENCES

1. Y.-K. Kim, K.-S. Kim, Y.-B. Song, J.H. Park, K.-A. Lee, 2.47 GPa grade ultra-strong 15Co-12Ni secondary hardening steel with superior ductility and fracture toughness, *Journal of Materials Science & Technology* 66 (2021) 36-45. <https://doi.org/10.1016/j.jmst.2020.06.014>.
2. J. Li, D. Zhan, Z. Jiang, H. Zhang, Y. Yang, Y. Zhang, Progress on improving strength-toughness of ultra-high strength martensitic steels for aerospace applications: a review, *Journal of Materials Research and Technology* 23 (2023) 172-190. <https://doi.org/10.1016/j.jmrt.2022.12.177>.
3. S. Hammarberg, J. Kajberg, S. Larsson, P. Jonsén, Ultra high strength steel sandwich for lightweight applications, *SN Appl. Sci.* 2 (2020) 1040. <https://doi.org/10.1007/s42452-020-2773-5>.
4. J. Zhao, Z. Jiang, Thermomechanical processing of advanced high strength steels, *Progress in Materials Science* 94 (2018) 174-242. <https://doi.org/10.1016/j.pmatsci.2018.01.006>.
5. R. Hörhold, M. Müller, M. Merklein, G. Meschut, Mechanical properties of an innovative shear-clinching technology for ultra-high-strength steel and aluminium in lightweight car body structures, *Weld World* 60 (2016) 613-620. <https://doi.org/10.1007/s40194-016-0313-0>.
6. T.B. Hilditch, T. De Souza, P.D. Hodgson, 2 - Properties and automotive applications of advanced high-strength steels (AHSS), in: *Welding and Joining of Advanced High Strength Steels (AHSS)*, 2015: pp. 9-28. <https://doi.org/10.1016/B978-0-85709-436-0.00002-3>.

7. R. Seede, D. Shoukr, B. Zhang, A. Whitt, S. Gibbons, P. Flater, A. Elwany, R. Arroyave, I. Karaman, An ultra-high strength martensitic steel fabricated using selective laser melting additive manufacturing: Densification, microstructure, and mechanical properties, *Acta Materialia* 186 (2020) 199-214. <https://doi.org/10.1016/j.actamat.2019.12.037>.
8. Y.H. Gao, S.Z. Liu, X.B. Hu, Q.Q. Ren, Y. Li, V.P. Dravid, C.X. Wang, A novel low cost 2000 MPa grade ultra-high strength steel with balanced strength and toughness, *Materials Science and Engineering: A* 759 (2019) 298-302. <https://doi.org/10.1016/j.msea.2019.05.039>.
9. J. Xue, Y. Zhang, W. Guo, M. Xia, J. Shi, G. Zhao, Q. Jia, H. Zhang, Significantly improving mechanical properties of ultra-high strength steel joints via optimal *in-situ* post-weld heat treatment, *Journal of Materials Processing Technology* 337 (2025) 118741. <https://doi.org/10.1016/j.jmatprotec.2025.118741>.
10. S. Chen, J. Zhu, T. Liu, Y. Liu, J. Xue, W. Zhang, G. Liu, Machine learning optimized by sparrow search for co-design of heat treatment process, microstructure, and properties in ultra-high-strength maraging steels, *Journal of Materials Research and Technology* 39 (2025) 8500-8511. <https://doi.org/10.1016/j.jmrt.2025.11.158>.
11. R. Ramprasad, R. Batra, G. Pilia, A. Mannodi-Kanakkithodi, C. Kim, Machine learning in materials informatics: recent applications and prospects, *Npj Comput Mater* 3 (2017) 54. <https://doi.org/10.1038/s41524-017-0056-5>.
12. Y. Su, H. Fu, Y. Bai, X. Jiang, J. Xie, Progress in Materials Genome Engineering in China, *Acta Metallurgica Sinica* 56 (2020) 1313-1323. <https://doi.org/10.11900/0412.1961.2020.00199>.
13. A. Agrawal, A. Choudhary, Perspective: Materials informatics and big data: Realization of the “fourth paradigm” of science in materials science, *APL Mater.* 4 (2016) 053208. <https://doi.org/10.1063/1.4946894>.
14. R.X. Yang, C.A. McCandler, O. Andriuc, M. Siron, R. Woods-Robinson, M.K. Horton, K.A. Persson, Big Data in a Nano World: A Review on Computational, Data-Driven Design of Nanomaterials Structures, Properties, and Synthesis, *ACS Nano* 16 (2022) 19873-19891. <https://doi.org/10.1021/acsnano.2c08411>.
15. D. Merayo, A. Rodríguez-Prieto, A.M. Camacho, Prediction of Physical and Mechanical Properties for Metallic Materials Selection Using Big Data and Artificial Neural Networks, *IEEE Access* 8 (2020) 13444-13456. <https://doi.org/10.1109/ACCESS.2020.2965769>.

16. S. Guo, J. Yu, X. Liu, C. Wang, Q. Jiang, A predicting model for properties of steel using the industrial big data based on machine learning, *Computational Materials Science* 160 (2019) 95-104. <https://doi.org/10.1016/j.commatsci.2018.12.056>.
17. Y. Yang, L. Zhao, C.-X. Han, X.-D. Ding, T. Lookman, J. Sun, H.-X. Zong, Taking materials dynamics to new extremes using machine learning interatomic potentials, *Jmi* 1 (2021). <https://doi.org/10.20517/jmi.2021.001>.
18. L.L. He, X.W. Chen, Z.H. Wang, Study on the penetration performance of concept projectile for high-speed penetration (CPHP), *International Journal of Impact Engineering* 94 (2016) 1-12. <https://doi.org/10.1016/j.ijimpeng.2016.03.010>.
19. N. Kılıç, S. Bedir, A. Erdik, B. Ekici, A. Taşdemirci, M. Güden, Ballistic behavior of high hardness perforated armor plates against 7.62mm armor piercing projectile, *Materials & Design* 63 (2014) 427-438. <https://doi.org/10.1016/j.matdes.2014.06.030>.
20. T. Børvik, S. Dey, L. Olovsson, Penetration of granular materials by small-arms bullets, *International Journal of Impact Engineering* 75 (2015) 123-139. <https://doi.org/10.1016/j.ijimpeng.2014.07.016>.
21. A. Manes, F. Serpellini, M. Pagani, M. Saponara, M. Giglio, Perforation and penetration of aluminium target plates by armour piercing bullets, *International Journal of Impact Engineering* 69 (2014) 39-54. <https://doi.org/10.1016/j.ijimpeng.2014.02.010>.
22. F. Zhu, Y. Chen, G. Zhu, Numerical simulation study on penetration performance of depleted Uranium (DU) alloy fragments, *Defence Technology* 17 (2021) 50-55. <https://doi.org/10.1016/j.dt.2020.01.002>.
23. L. Mao, W. Zhao, C. Liu, Z. Pang, Z. Du, Fracture and damage evolution of metal molybdenum based on a modified Johnson-Cook model under high-temperature conditions, *International Journal of Impact Engineering* 212 (2026) 105663. <https://doi.org/10.1016/j.ijimpeng.2026.105663>.
24. H. Zhipeng, G. Lihong, W. Yangwei, W. Fuchi, Determination of the Johnson-Cook Constitutive Model Parameters of Materials by Cluster Global Optimization Algorithm (vol 25%2C pg 4099%2C 2016), *Journal of Materials Engineering and Performance* 25 (2016) 4108. <https://doi.org/10.1007/s11665-016-2256-4>.
25. R.M. May, Simple mathematical models with very complicated dynamics, *Nature* 261 (1976) 459-467. <https://doi.org/10.1038/261459a0>.
26. T. Geisel, V. Fairen, Statistical properties of chaos in Chebyshev maps, *Physics Letters A* 105 (1984) 263-266. [https://doi.org/10.1016/0375-9601\(84\)90993-9](https://doi.org/10.1016/0375-9601(84)90993-9).

27. D. He, C. He, L.-G. Jiang, H.-W. Zhu, G.-R. Hu, Chaotic characteristics of a one-dimensional iterative map with infinite collapses, *IEEE Transactions on Circuits and Systems I: Fundamental Theory and Applications* 48 (2001) 900-906. <https://doi.org/10.1109/81.933333>.
28. D. Yang, G. Li, G. Cheng, On the efficiency of chaos optimization algorithms for global optimization, *Chaos, Solitons & Fractals* 34 (2007) 1366-1375. <https://doi.org/10.1016/j.chaos.2006.04.057>.
29. A. Shrot, M. Bäker, Determination of Johnson-Cook parameters from machining simulations, *Computational Materials Science* 52 (2012) 298-304. <https://doi.org/10.1016/j.commatsci.2011.07.035>.
30. Z. Zeng, W. Liang, T. Wang, Z. Hong, Q. Chang, S. Yang, A method for predicting the capacity of lithium-ion batteries based on Pearson correlation coefficient-guided multi-objective particle swarm optimization, *Computers & Industrial Engineering* 210 (2025) 111514. <https://doi.org/10.1016/j.cie.2025.111514>.

Accepted Article

Supplementary Materials

Supplementary Tables

Table S1. Heat treatment process design and expected primary microstructure details

ID	Heat Treatment Process	Expected Primary Microstructure
1	900°C/1h+OQ	
2	1000°C/1h+OQ	Martensite
3	1100°C/1h+OQ	
4	850°C/1h+OQ+200°C/2h+AC	Tempered Martensite
5	900°C/1h+OQ+200°C/2h+AC	
6	900°C/1h+OQ+400°C/2h+AC	Tempered Martensite, Troostite
7	900°C/1h+OQ+600°C/2h+AC	Tempered Martensite, Sorbite
8	950°C/1h+OQ+200°C/2h+AC	Tempered Martensite
9	1000°C/1h+OQ+200°C/2h+AC	
10	1000°C/1h+OQ+400°C/2h+AC	Tempered Martensite, Troostite
11	1000°C/1h+OQ+600°C/2h+AC	Tempered Martensite, Sorbite
12	1050°C/1h+OQ+200°C/2h+AC	Tempered Martensite
13	1100°C/1h+OQ+200°C/2h+AC	
14	1100°C/1h+OQ+400°C/2h+AC	Tempered Martensite, Troostite
15	1100°C/1h+OQ+600°C/2h+AC	Tempered Martensite, Sorbite
16	1100°C/1h+355°C/30h+OQ	Upper Bainite
17	1100°C/1h+345°C/30h+OQ	
18	1100°C/1h+265°C/10h+OQ	
19	1100°C/1h+255°C/10h+OQ	
20	1100°C/1h+265°C/20h+OQ	Lower Bainite
21	1100°C/1h+265°C/30h+OQ	
22	900°C/1h+265°C/10h+OQ	
23	900°C/1h+265°C/20h+OQ	

ID	Heat Treatment Process	Expected Primary Microstructure
24	1000°C/1h+265°C/10h+OQ	
25	1000°C/1h+265°C/20h+OQ	
26	850°C/1h+OQ+-73°C/1h+200°C/2h+AC	
27	900°C/1h+OQ+-73°C/1h+200°C/2h+AC	
28	950°C/1h+OQ+-73°C/1h+200°C/2h+AC	
29	1000°C/1h+OQ+-73°C/1h+200°C/2h+AC	Tempered Martensite
30	1050°C/1h+OQ+-73°C/1h+200°C/2h+AC	
31	1100°C/1h+OQ+-73°C/1h+200°C/2h+AC	
32	1100°C/1h+OQ+-73°C/1h+260°C/2h+AC	
33	1100°C/1h+OQ+-73°C/1h+300°C/2h+AC	
34	1100°C/1h+OQ+-73°C/1h+400°C/2h+AC	Tempered Martensite, Troostite
35	1100°C/1h+OQ+-73°C/1h+400°C/5h+AC	
36	1100°C/1h+OQ+-73°C/1h+482°C/2h+AC	
37	1100°C/1h+OQ+-73°C/1h+482°C/5h+AC	
38	1100°C/1h+OQ+-73°C/1h+500°C/2h+AC	
39	1100°C/1h+OQ+-73°C/1h+560°C/2h+AC	Tempered Martensite, Sorbite
40	1100°C/1h+OQ+-73°C/1h+560°C/5h+AC	
41	1100°C/1h+OQ+-73°C/1h+600°C/2h+AC	
42	1100°C/1h+OQ+-73°C/1h+700°C/2h+AC	
43	900°C/1h+OQ+-73°C/1h+260°C/2h+AC	Tempered Martensite, Troostite
44	900°C/1h+OQ+-73°C/1h+300°C/2h+AC	
45	900°C/1h+OQ+-73°C/1h+400°C/2h+AC	
46	900°C/1h+OQ+-73°C/1h+400°C/5h+AC	
47	900°C/1h+OQ+-73°C/1h+482°C/2h+AC	Tempered Martensite, Sorbite
48	900°C/1h+OQ+-73°C/1h+482°C/5h+AC	
49	900°C/1h+OQ+-73°C/1h+500°C/2h+AC	

ID	Heat Treatment Process	Expected Primary Microstructure
50	900°C/1h+OQ+-73°C/1h+560°C/2h+AC	
51	900°C/1h+OQ+-73°C/1h+560°C/5h+AC	
52	900°C/1h+OQ+-73°C/1h+600°C/2h+AC	
53	900°C/1h+OQ+-73°C/1h+700°C/2h+AC	
54	1100°C/15h+FC	
55	1050°C/15h+FC	
56	1000°C/15h+FC	Pearlite
57	950°C/1h+FC	
58	900°C/1h+FC	
59	850°C/1h+FC	
60	850°C/1h+WQ+610°C/5h+AC	Tempered Martensite, Sorbite
61	790°C/5h+FC	
62	730°C/5h+FC	Pearlite
63	670°C/5h+FC	
64	850°C/1h+AC	
65	850°C/1h+WQ	
66	1000°C/1h+WQ	Martensite
67	1100°C/1h+WQ	
68	900°C/1h+WQ	
69	900°C/1h+WQ+200°C/2h+AC	Tempered Martensite
70	900°C/1h+WQ+400°C/2h+AC	Tempered Martensite, Troostite
71	900°C/1h+WQ+600°C/2h+AC	Tempered Martensite, Sorbite
72	1000°C/1h+WQ+200°C/2h+AC	Tempered Martensite
73	1000°C/1h+WQ+400°C/2h+AC	Tempered Martensite, Troostite
74	1000°C/1h+WQ+600°C/2h+AC	Tempered Martensite, Sorbite
75	1100°C/1h+WQ+200°C/2h+AC	Tempered Martensite

ID	Heat Treatment Process	Expected Primary Microstructure
76	1100°C/1h+WQ+400°C/2h+AC	Tempered Martensite, Troostite
77	1100°C/1h+WQ+600°C/2h+AC	Tempered Martensite, Sorbite
78	1100°C/1h+OQ+-73°C/1h+200°C/4h+AC	
79	1050°C/1h+OQ+-73°C/2h+200°C/2h+AC	
80	1100°C/1h+OQ+-73°C/2h+200°C/2h+AC	
81	1150°C/1h+OQ+-73°C/1h+200°C/2h+AC	
82	1150°C/1h+OQ+-73°C/2h+200°C/2h+AC	Tempered Martensite
83	1050°C/1h+OQ+-73°C/1h+200°C/4h+AC	
84	1150°C/1h+OQ+-73°C/2h+200°C/4h+AC	
85	850°C/1h+WQ+150°C/5h+AC	
86	850°C/1h+WQ+200°C/5h+AC	
87	850°C/1h+WQ+250°C/5h+AC	
88	850°C/1h+WQ+350°C/5h+AC	
89	850°C/1h+WQ+400°C/5h+AC	Tempered Martensite, Troostite
90	850°C/1h+WQ+450°C/5h+AC	
91	850°C/1h+WQ+500°C/5h+AC	
92	850°C/1h+WQ+600°C/5h+AC	Tempered Martensite, Sorbite
93	850°C/1h+WQ+650°C/5h+AC	
94	790°C/5h+WQ	
95	730°C/5h+WQ	Ferrite + Martensite
96	670°C/5h+WQ	
97	1100°C/1h+OQ+200°C/2h+AC+-73°C/1h+AC	
98	1100°C/1h+OQ+200°C/2h+- 73°C/1h+200°C/2h+AC	Tempered Martensite
99	1100°C/1h+OQ+-73°C/1h+200°C/6h+AC	
100	1100°C/1h+OQ+-73°C/1h+200°C/8h+AC	
101	900°C/1h+OQ+300°C/2h+AC	Tempered Martensite, Troostite

ID	Heat Treatment Process	Expected Primary Microstructure
102	900°C/1h+OQ+500°C/2h+AC	Tempered Martensite, Sorbite
103	1000°C/1h+OQ+300°C/2h+AC	Tempered Martensite, Troostite
104	1000°C/1h+OQ+500°C/2h+AC	Tempered Martensite, Sorbite
105	1100°C/1h+OQ+300°C/2h+AC	Tempered Martensite, Troostite
106	1100°C/1h+OQ+500°C/2h+AC	Tempered Martensite, Sorbite
107	900°C/1h+WQ+300°C/2h+AC	Tempered Martensite, Troostite
108	900°C/1h+WQ+500°C/2h+AC	Tempered Martensite, Sorbite
109	1000°C/1h+WQ+300°C/2h+AC	Tempered Martensite, Troostite
110	1000°C/1h+WQ+500°C/2h+AC	Tempered Martensite, Sorbite
111	1100°C/1h+WQ+300°C/2h+AC	Tempered Martensite, Troostite
112	1100°C/1h+WQ+500°C/2h+AC	Tempered Martensite, Sorbite
113	1100°C/1h+OQ+-73°C/1h+550°C/2h+AC	Tempered Martensite, Sorbite
114	900°C/0.5h+OQ+200°C/2h+AC	
115	1000°C/0.5h+OQ+200°C/2h+AC	Tempered Martensite
116	1100°C/0.5h+OQ+200°C/2h+AC	
117	1100°C/0.5h+OQ+400°C/2h+AC	Tempered Martensite, Troostite
118	1100°C/0.5h+OQ+-73°C/1h+200°C/2h	Tempered Martensite
119	1100°C/1h+OQ+200°C/2h+AC+200°C/2h+AC	
120	1100°C/1h+OQ+300°C/2h+AC+300°C/2h+AC	Tempered Martensite, Troostite
121	1100°C/1h+OQ+400°C/2h+AC+400°C/2h+AC	
122	950°C/1h+WQ	Martensite
123	1050°C/1h+WQ	
124	850°C/1h+WQ+550°C/5h+AC	Tempered Martensite, Sorbite
125	700°C/5h+WQ	Martensite
126	1000°C/1h+WQ+150°C/5h+AC	Tempered Martensite
127	1000°C/1h+WQ+200°C/5h+AC	

ID	Heat Treatment Process	Expected Primary Microstructure
128	1000°C/1h+WQ+250°C/5h+AC	
129	1000°C/1h+WQ+350°C/5h+AC	
130	1000°C/1h+WQ+400°C/5h+AC	Tempered Martensite, Troostite
131	1000°C/1h+WQ+450°C/5h+AC	
132	1000°C/1h+WQ+500°C/5h+AC	
133	1000°C/1h+WQ+600°C/5h+AC	Tempered Martensite, Sorbite
134	1000°C/1h+WQ+650°C/5h+AC	

Note: AC: Air cooling. OQ: Oil quenching. WQ: Water quenching

Table S2. Mechanical properties dataset of G33 ultra high strength steel

Test Type	Performance Parameter	Units
Quasi-static Tensile Test	Yield Strength	MPa
	Tensile Strength	MPa
	Total Elongation at Fracture	%
Quasi-static Compression Test	Yield Strength	MPa
	Compressive Strength	MPa
Vickers Hardness Test	Vickers Hardness	HRC
Dynamic Tensile Test at 2000/s	Yield Strength	MPa
	Tensile Strength	MPa
	Total Elongation at Fracture	%
Dynamic Compression Test at 3000/s	Yield Strength	MPa
	Compressive Strength	MPa
Dynamic Compression Test at 5000/s	Yield Strength	MPa
	Compressive Strength	MPa

Table S3. Service performance dataset of G33 ultra high strength steel

Test Type	Performance Parameter	Unit
G33 Ultra-High Strength Steel Projectile Penetration Test	Penetration Speed	m/s
	Projectile Penetration (Yes/No)	/

Test Type	Performance Parameter	Unit
	Integrity of Projectile Post-Penetration	/
	Residual Velocity Post-Penetration	m/s
	Critical Projectile Fracture Penetration Velocity	m/s

Table S4. Grid parameter definition

	param_grid
n_estimators	100, 200, 500
max_features	Sqrt, 0.5
max_depth	None, 10, 20, 30
min_samples_split	2, 5, 10
min_samples_leaf	1, 2, 4

Table S5. Initial parameter settings of the MLP regression model

Layer	Parameter	Activation Function
Input Layer	128	ReLU
Hidden Layer	64	ReLU
Output Layer	1	

Supplementary Figures

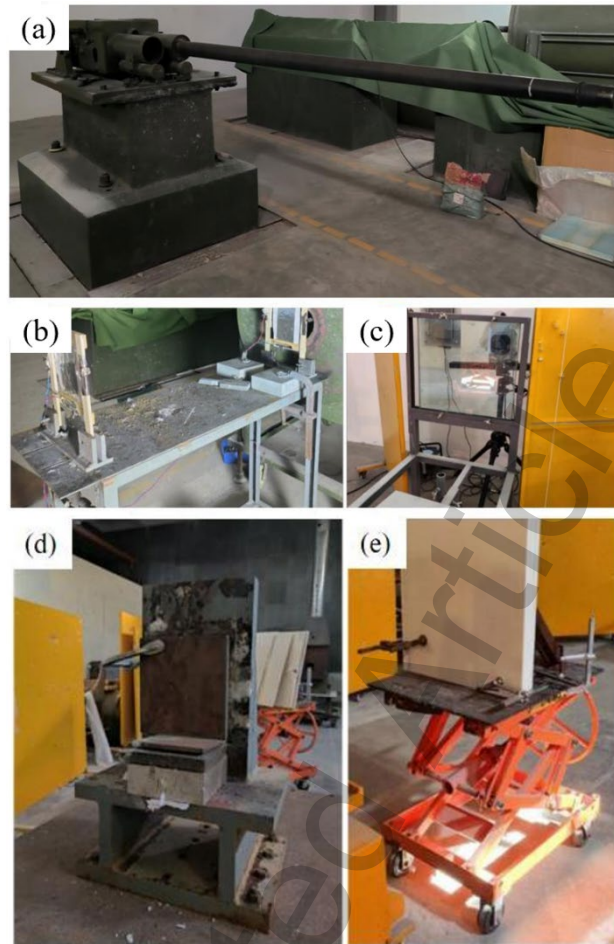


Fig. S1. (a) 30-37 smoothbore cannon; (b) Foil interrupt target; (c) High-speed camera; (d) Target stand; (e) After-effect target stand and recovery mat(photographs by the authors).

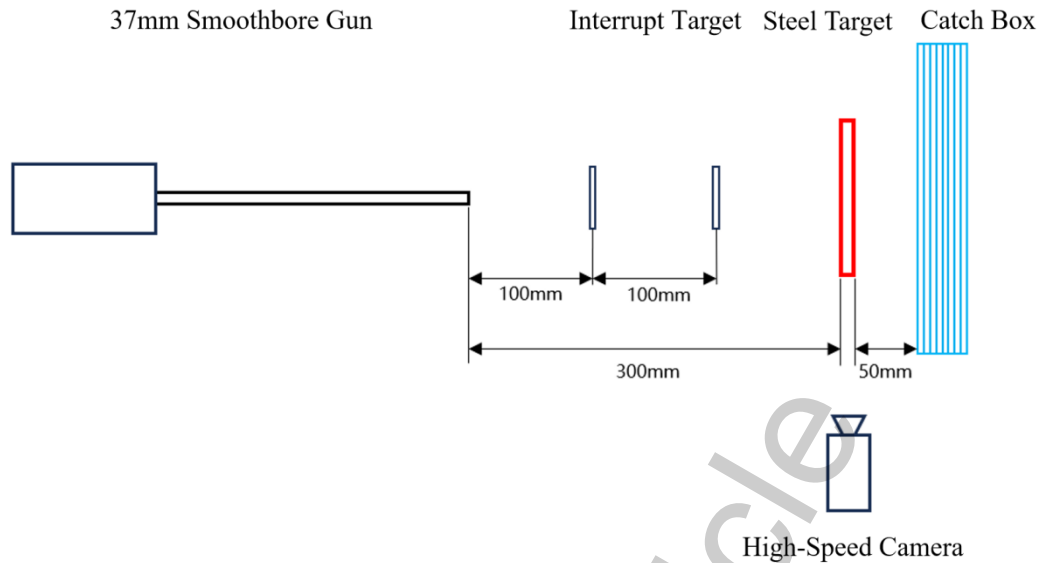


Fig. S2. Schematic diagram of scaled projectile penetration test

The dynamic tensile properties of ultra-high-strength steel are accurately determined using a Split Hopkinson Tension Bar (SHTB). Within the SHTB system, both the incident and transmission bars, fabricated from 55CrSi alloy steel, measure 14.5mm in diameter, with lengths of 2000mm and 1000mm respectively. The test specimen, with a gauge section of $\Phi 2 \times 5$ mm, is securely connected to the loading bars (keyword: `*CONTACT_TIDE_SURFACE_TO_SURFACE`). To eliminate potential effects from boundary conditions such as the impact velocity on the SHTB loading simulation system, the incident wave recorded during experimental testing is applied as stress at the end face of the incident bar. The loading bars are modeled using a linear elastic constitutive model, while the specimen is described by the Johnson-Cook constitutive and failure model (keyword: `*MAT_JOHNSON_COOK`). To streamline the computational effort, a quarter-scale model is employed, as depicted in Fig S3(a).

The quasi-static tensile properties of ultra-high-strength steel are determined using an electronic universal testing machine, with the simulation accurately modeled to reflect the precise dimensions of the actual equipment. The specimen measures a total length of 65mm, including a gauge section 30mm long and 5mm in diameter. Constraints are strategically placed at both ends of the specimen to replicate experimental conditions. Specifically, two layers of elements at one end of the specimen create a robust connection with the loading bar (keyword: `*CONTACT_TIDE_SURFACE_TO_SURFACE`) and are configured as rigid bodies (keyword: `*SECTION_SOLID`) to simulate the clamping effects typically provided by testing fixtures. A single node on the rigid body is set to impose a displacement velocity along the direction of tension (keyword: `*BOUNDARY-PRESCRIBED_MOTION_NODE`), thus controlling the strain rate of the specimen at 1×10^{-3} /s. A fixed constraint is also applied at the base of the specimen (keyword: `*BOUNDARY_SPC_SET`) to emulate the restraint provided by test fixtures during

actual experiments. The specimen employs the Johnson-Cook constitutive and failure model (keyword: *MAT_JOHNSON_COOK) for its material characterization. To streamline the computational efforts, a quarter-scale model is employed, as depicted in Fig S3(b).

To facilitate the automatic extraction of simulation results, the simulation model undergoes specific preprocessing steps. In the Split Hopkinson Tension Bar (SHTB) simulations, circumferential elements at the midpoint between the incident and transmission bars—where resistive strain gauges are typically attached—are designated as a solid element set (keyword: *SET_SOLID). During the simulation, the "stress-time" profiles for these elements along the loading direction are captured and recorded in the elout file (keyword: *DATABASE_HISTORY_SOLID_SET). After the simulation concludes, data from the elout file are extracted to compute the "strain-time" curves for the sets of elements in both the incident and transmission bars. Finally, applying the principles of the three-wave method, the stress-strain curves of the material are calculated.

In simulations of quasi-static tensile tests, two symmetrical nodes are strategically placed along the loading direction on the surface of the specimen (keyword: *SET_NODE_LIST). This setup is intended to replicate the tracking of marked positions by an extensometer during experimental tests. Throughout the simulation, the "position-time" data for these nodes are recorded in the nodeout file. Subsequent extraction and analysis of this data yield the "strain-time" curve for ultra-high-strength steel. Additionally, the last three layers of elements positioned away from the loading direction are grouped into a solid element set (keyword: *SET_SOLID). During the simulation, "stress-time" profiles for these elements are captured in the elout file (keyword: *DATABASE_HISTORY_SOLID_SET). Post-simulation, this data is extracted to compute the "stress-time" curve of the specimen. This analysis culminates in the derivation of the "stress-strain" curve for ultra-high-strength steel under experimental conditions, providing critical insights into material behavior under tensile loading.

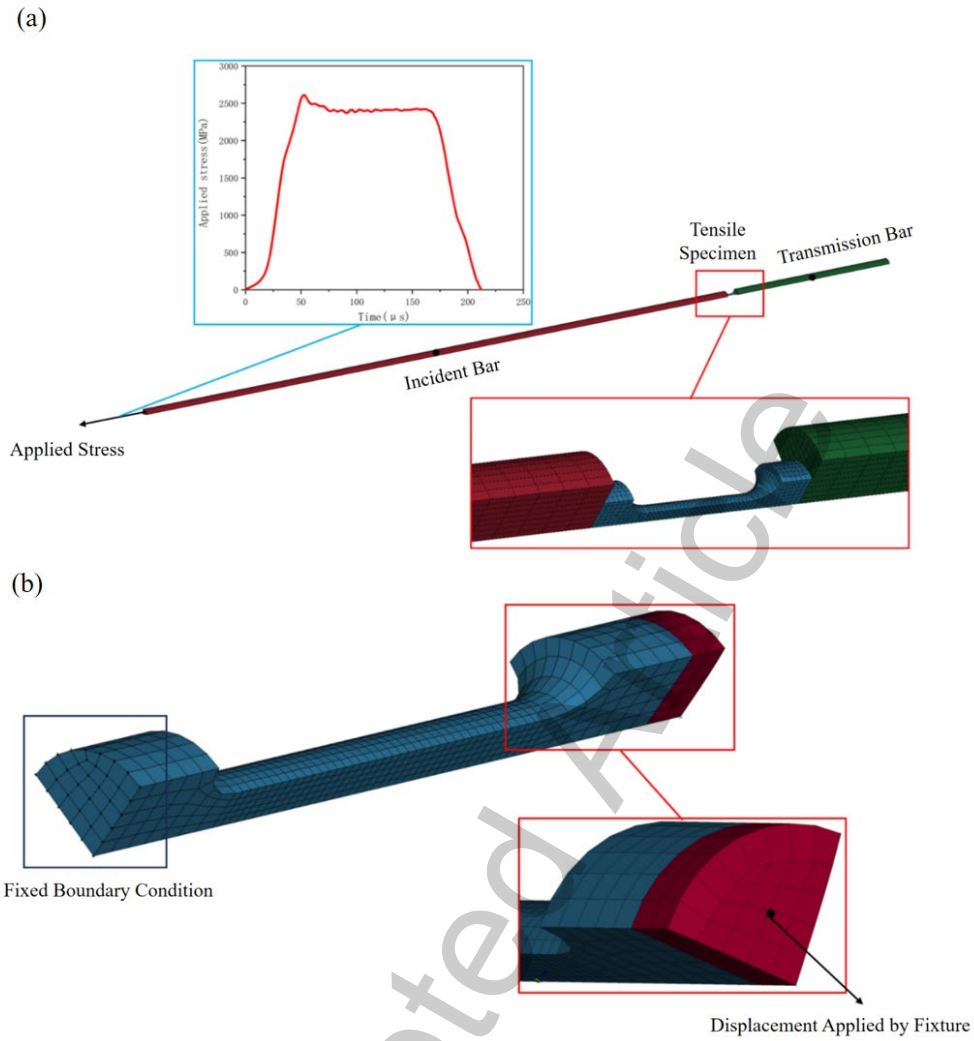


Fig. S3. (a) Numerical simulation model of dynamic tensile test; (b) Numerical simulation model of quasi-static tensile test

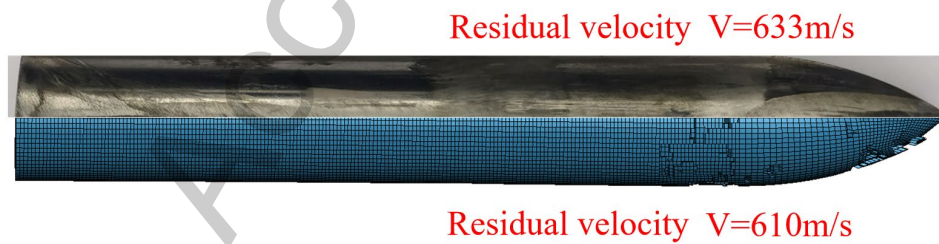


Fig. S4. Comparison between experimental results and numerical simulation results

Classification Performance Comparison

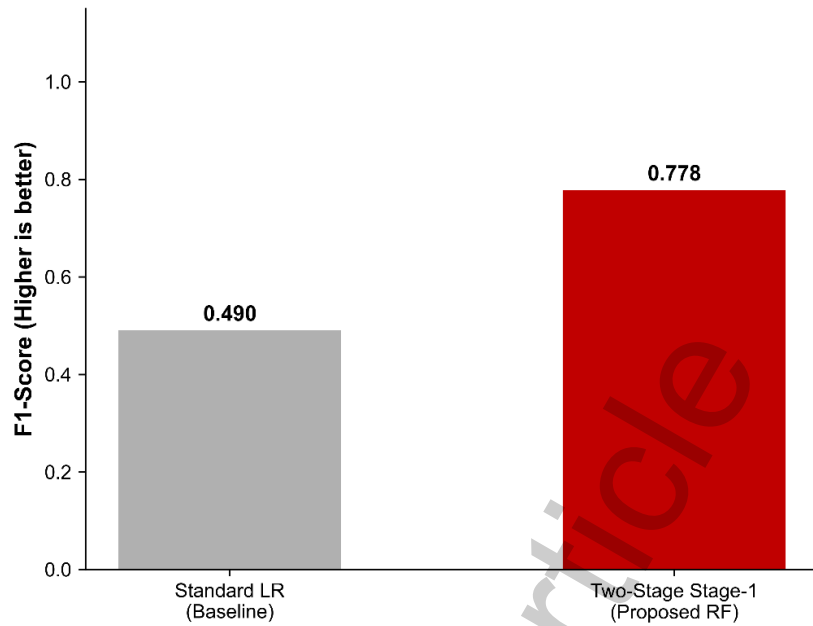


Fig. S5. Performance comparison of the proposed Two-Stage framework against Single-Stage baselines. Classification F1-score comparison for predicting the ballistic limit boundary (penetration occurrence).

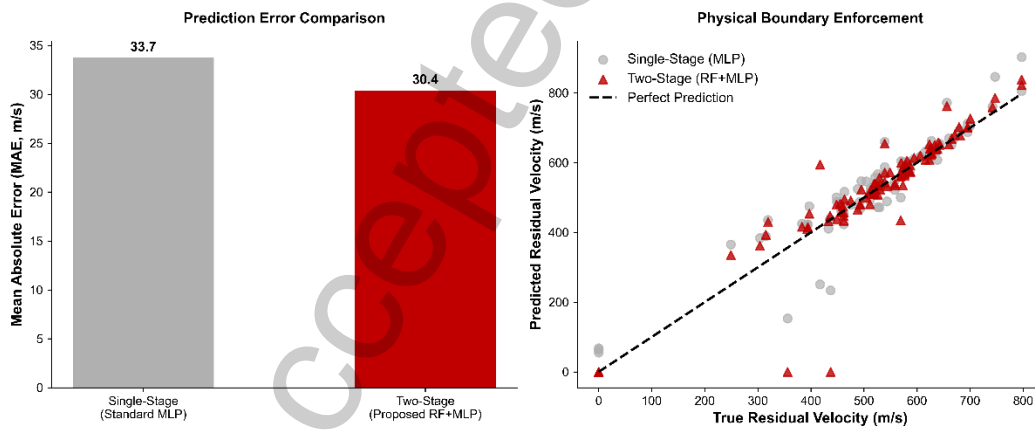


Fig. S6. Regression Mean Absolute Error (MAE) and physical boundary enforcement for predicting post-failure residual velocity, demonstrating the elimination of zero-boundary anomalies.

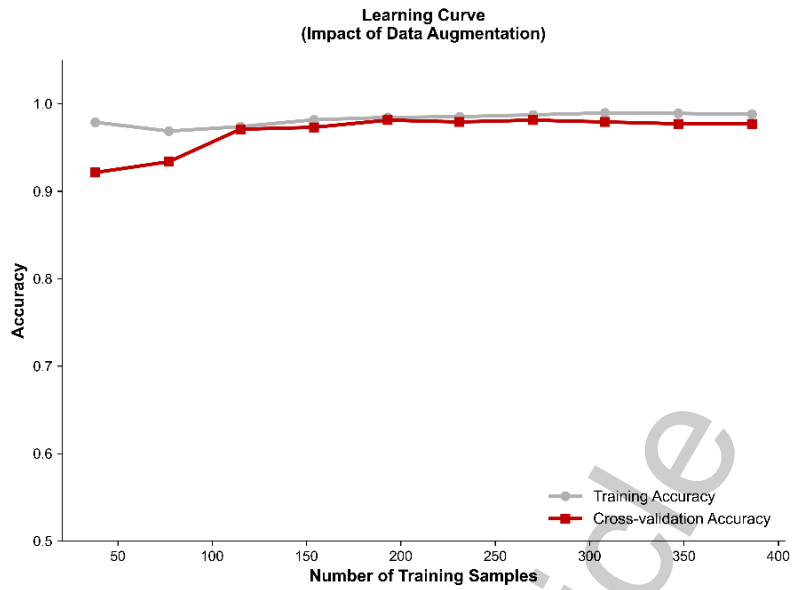


Fig. S7. Learning curve demonstrating the impact of simulation-based data augmentation. The trajectory of cross-validation accuracy versus training sample size explicitly proves that standard data-driven mappings suffer from underfitting and severe variance under limited initial experimental data (<100 samples), and successfully plateau only after high-throughput simulation augmentation.

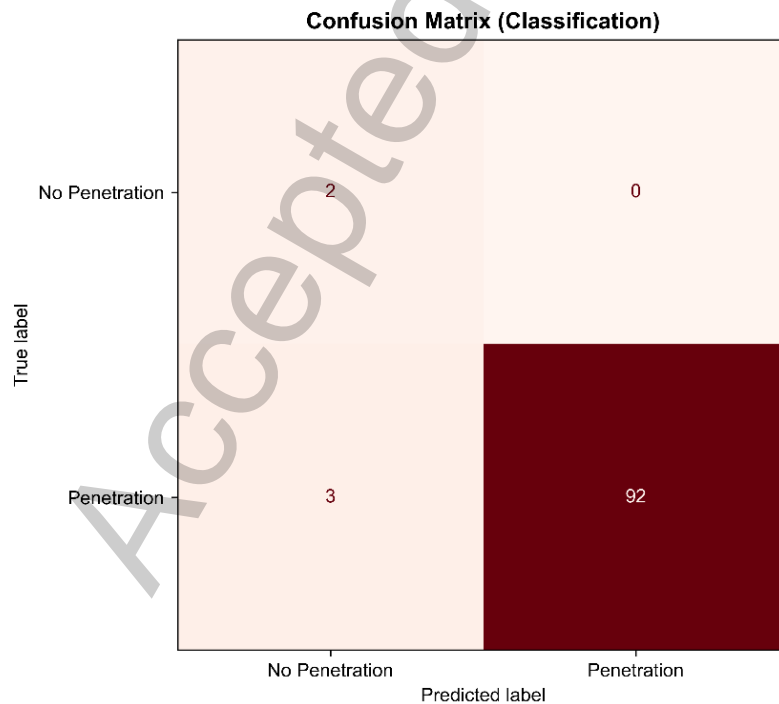


Fig. S8. Confusion matrix evaluating the predictive accuracy of the Stage-1 Random Forest classifier. The matrix shows a highly balanced and precise classification of the physical threshold (penetration vs. non-penetration) evaluated on the test set.

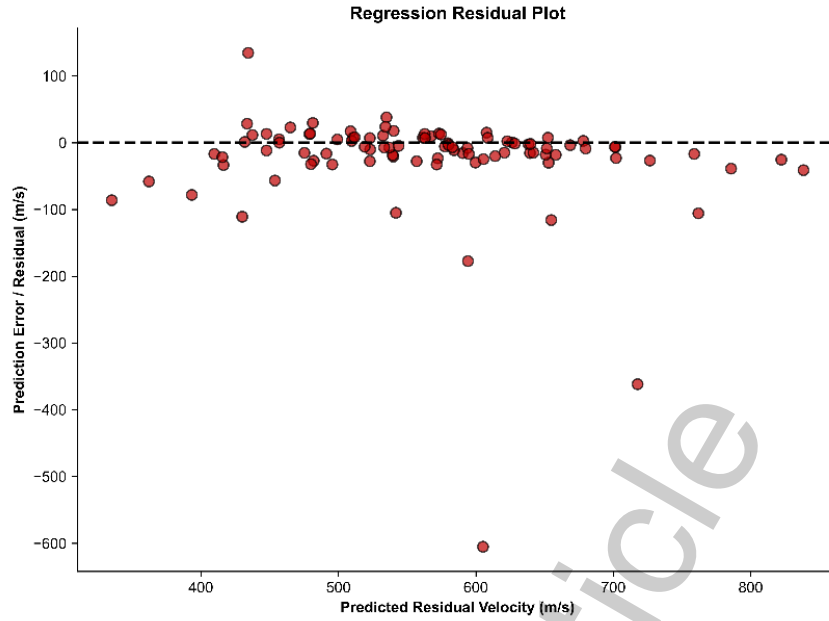


Fig. S9. Regression residual plot for the Stage-2 MLP model. The plot displays the distribution of prediction errors for penetrated targets, confirming that the residuals are homoscedastic and normally distributed around the zero-error baseline without systematic bias.

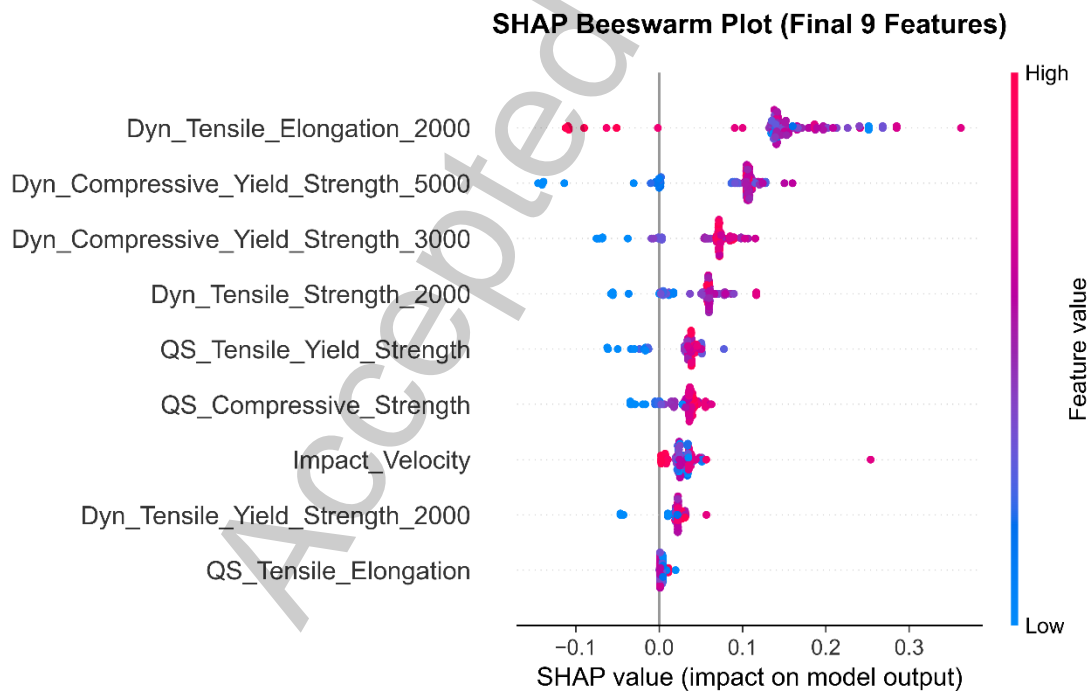


Fig. S10. SHAP (SHapley Additive exPlanations) summary beeswarm plot illustrating global feature importance. The plot reveals the relative contribution and physical impact directions of various mechanical features on the penetration occurrence, highlighting the dominant roles of impact velocity, dynamic yield strength, and quasi-static elongation.